Unravelling the magma feeding system of a young basaltic oceanic volcano

Vittorio Zanon[1,2], Adriano Pimentel[1,3], Marion Auxerre[4], Greta Marchini[1], Finlay M. Stuart[5]

[1] Instituto de Investigação em Vulcanologia e Avaliação de Riscos (IVAR), Universidade dos Açores, Rua Mãe de Deus, 9500-123 Ponta Delgada, Portugal,
Vittorio.VZ.Zanon@azores.gov.pt

[2] Institut de Physique du Globe de Paris, Université de Paris, CNRS UMR-7154, Paris 75005, France

[3] Centro de Informação e Vigilância Sismovulcânica dos Açores (CIVISA), Rua Mãe de Deus, 9500-123 Ponta Delgada, Portugal, Adriano.HG.Pimentel@azores.gov.pt

[4] Centre de Recherche Pétrologiques et Géochimiques (CRPG), 54501 Vandoeuvre-lès-Nancy, France

[5] Scottish Universities Environmental Research Centre (SUERC), Rankine Avenue Scottish Enterprise Technology Park, East Kilbride, G75 0QF, United Kingdom

Abstract

A multidisciplinary approach combining petrological, geochemical, and fluid-inclusion studies with seismic monitoring data was used to build a model of the magma feeding system of Pico volcano (Azores islands, North Atlantic Ocean). We explore how magma has ascended to the surface in the last 10 ka and how this ascent is associated with the selective activation of the three tectonic systems intersecting the volcano. The deepest and most important ponding level for all ascending magmas is located at 17.3-17.7 km and corresponds to the Moho Transition Zone (MTZ), which marks the transition from mantle rocks to ultramafic cumulates. At shallower depth ascending magmas carry > 30 vol% of clinopyroxene and olivine. Each magma ascent followed a distinct path and ponded often for a limited period. Ponding levels common to all feeding systems are present at 16.3-16.7 km, 12.1-14.5 km, 9.4-9.8 km, and 7.7-8.1 km. These depths mark important discontinuities where magmas formed stacked sills and evolved through fractional crystallisation. Dense and un-decrepitated fluid inclusions show rapid ascent from the MTZ along the Lomba do Fogo-São João fault (N150° system) and along the N120° regional transtensive system, despite multiple intrusions. Magma ponding at 5.6-6.8 km occurs where the N150° and N60° tectonic systems intersect each other. Here magma evolves towards plagioclase-rich and is only erupted at the summit crater and subterminal vents. This region is the source of the frequent microseismicity recorded at 4 to 7 km beneath the southern flank of Pico volcano, which might be associated with the early stages of formation of a more complex magma reservoir. The local and regional tectonics are of paramount importance in the activation of the different magma feeding systems over time. This new information is fundamental to improve the knowledge on the future eruptive behaviour of Pico volcano and can have significant implications on the mitigation of volcanic risk. This multidisciplinary approach can be applied not only to other volcanoes of the Azores but also to poorly monitored oceanic volcanoes, where magma ascent strongly depends on the activation of tectonic systems.

Keywords

fluid inclusions; tectonic systems; magma ascent; oceanic island; Pico volcano

1. Introduction

Tracking magma movement relies on geophysical, geodetic and geochemical monitoring techniques that detect the effects of magma interacting with surrounding rocks and fluids at depth, providing the first warning of volcanic unrest (e.g., Sparks, 2003; Sparks et al., 2012). However, even robust monitoring networks deployed on active volcanoes may fail to predict eruptive behaviour, such as the cases of the 1993 Mt. Galeras eruption, Colombia (Baxter and Gresham, 1997), the 2004 Mt. Etna eruption, Italy (Corsaro and Miraglia, 2005), the 2014 Mt. Ontake eruption, Japan (Sano et al., 2015), and the 2019 repeated paroxysmal explosive events at Stromboli volcano (Italy). This has significant risk implications, in particular with dormant volcanoes and those with low eruption frequency. Petrological modelling of recent eruptions can provide vital information on the magma plumbing systems, in particular the depths where magmas pond and/or are stored, and their ascent paths to the surface.

The magmatic systems of oceanic volcanoes are characterized by multiple, stacked areas where magma can be temporarily or definitely stored between subsolidus material (e.g., Hansteen et al., 1998; Schwarz et al., 2004; Klügel et al., 2005; Stroncik et al., 2009; Boudoire et al., 2019; White et al., 2019). The location and geometry of magma feeding systems is determined by many conditions, however while dykes are the main means of vertical transport, sheet intrusions and sills are the most probable magma storage sites in extensional settings (e.g. Huang et al., 2015). Repeated magma intrusions in a short time frame might lead to the formation of a more complex magma reservoir (Carrara et al., 2019).

The development of complex and long-lived magma reservoirs is related to the ageing of magmatic systems. Magma reservoirs are now considered to be “crystal mushes” (e.g., Hildreth and Wilson, 2007; Bachmann and Bergantz, 2008; Carrara et al., 2019; Sparks et al., 2019), spatially limited regions of the crust/mantle with variable proportions of coexisting melt, crystals and exsolved volatiles. Melt is present in a few tens of percent at most (Lees, 2007; Huang et al., 2015; Kiser et al., 2016) and coexists with crystals which may be dispersed or form a stiff framework (mush) at the edges of the magmatic system (Wager et al., 1960). The crystal component increases in volume with time and becomes an important feature of the magmatic system.

The volcanism of the Azores islands (North Atlantic Ocean) developed in two distinct phases (Zanon, 2015a). In the first phase, lasting for one million years or more, basalts erupted through fissures originating elongated volcanic ridges. In the second phase, and where the regional transtensive tectonic systems were intersected by local faults, shallow magma reservoirs were able to develop, leading to the formation of centralised-feeding systems and central volcanoes (e.g., Miranda et al., 1998; Queiroz et al., 2015). The magmatic systems of Azorean central volcanoes share similar characteristics: a) a main storage area at the Moho Transition Zone (MTZ), overlain by crystal mush/cumulate layers with thicknesses ranging from several hundreds of metres to kilometres; b) multiple ephemeral intrusive layers, probably feeding only a few eruptions; c) magma ascent dynamics linked to the activation of transtensive faults; and d) low erupted volumes and magma output rates (Zanon and Frezzotti, 2013; Zanon and Pimentel, 2015). These characteristics limit our ability to investigate this type of magma feeding systems with common monitoring techniques, thus it is fundamental to improve our understanding through the detailed study of recent volcanic products.

Pico is a young basaltic oceanic volcano in the Azores archipelago. This central volcano grew rapidly over the last 50 ka superimposed on an older basaltic ridge that is intersected by transtensive faults (Madeira and Brum da Silveira, 2003; Marques et al., 2013). The numerous cones on the flanks provide evidence for recurrent activity during the Holocene. In historical times (i.e., since the late 15th century) the volcano erupted in 1718 and 1720 through lateral fissures.

Pico volcano is an ideal site to investigate the development of magma feeding systems at young oceanic volcanoes. Here we report integrated petrological, geochemical, and fluid-inclusion studies and combine with seismic monitoring data to build a model of the magma feeding system beneath this volcano. The insights gained in this work provide a better understanding of the future eruptive behaviour of Pico volcano and may also apply to other young basaltic oceanic volcanoes.

2. Geological setting

The islands of the Azores in the North Atlantic Ocean are the emerged portions of large sub-parallel volcanic ridges that rise from the Azores plateau. This region is marked by major tectonic structures: the Mid-Atlantic Ridge, the Terceira Rift and the East Azores Fracture Zone. The Mid-Atlantic Ridge separates the Eurasian and Nubian lithospheric plates, to the east, from the North American plate, to the west. The Terceira Rift corresponds to the northern spreading system of the diffuse boundary between the Eurasian and Nubian plates (inset of Fig. 1). For a detailed review of the Azores geodynamic setting see Gente et al. (2003), Vogt and Jung (2004), Georgen and Sankar (2010), Marques et al. (2013), Miranda et al. (2014) and Trippanera et al. (2014).

Pico Island together with the neighbouring island of Faial are the main geomorphological features of the large Pico-Faial volcanic ridge. The emerged portion of the ridge is 70 km long and results from the interplay between fissure volcanism, central volcanoes and tectonic structures along a ~N120° spreading system (e.g., Zanon and Frezzotti, 2013; Silva et al., 2018). Faial Island is dominated by the Caldeira central volcano, which is in a mature stage of evolution, erupting trachytic magmas during the Holocene (Pimentel et al., 2015). In contrast, the adjacent Capelo fissure zone only erupted mafic magmas in the same period. Faial is cut by a WNW-ESE fault system (Trippanera et al., 2014) that extends offshore eastwards to Pico Island.

Pico is the youngest island of the Azores archipelago (270 ±150 ka; Demande et al., 1982) and is composed by three volcanic systems: Topo volcano, Planalto da Achada fissure zone and Pico volcano (Fig. 1). Topo is only exposed in the southern part of the island, it is an extinct volcano, deeply eroded, dissected by faults, and covered by younger volcanic products. Planalto da Achada fissure zone is a 30 km long N120°-trending ridge of cinder cones. Lava flows partially overlap the Topo edifice and are intercalated with basalts from Pico volcano to the west. This fissure zone last erupted in 1562-64 (Nunes, 1999; Madeira and Brum da Silveira, 2003; Costa et al., 2015).

Pico central volcano is the youngest of the Azores (K/Ar age of 53 ±5 ka; Costa et al., 2014), although its true base has never been dated. It erupted frequently during the Holocene and at least 22 times in the last 1,500 years (Nunes, 1999). Since the island's settlement in late 15th century it has erupted twice; in 1718 along a N150° fault that cross-cuts the entire edifice, and in 1720 along a radial fissure in the southeast. The base of Pico volcano is a shield edifice with gentle slopes (up to 10°) punctuated by many recent cinder cones and hornitos. The volcano rises to 2,351 m above sea level as an almost perfect conical shape with steep slopes (up to 40°) and without lateral cones above 1,500 m a.s.l. (Fig. 1). The summit is truncated by a 550 m-wide sub-circular pit-crater, partially occupied by a 110 m-high hornito (Piquinho) and intersected by a N60°-trending eruptive fissure.

Recent eruptions (≤10 ka) occurred along three main tectonic directions (Fig. 1): a) the regional transtensive trend that crosses the entire island with a general N120° direction. It is expressed by the alignment of large cinder cones of Planalto da Achada fissure zone, on the eastern side of the island, and by sparse cinder cones and hornitos of smaller size on the western flank of Pico volcano. This trend is offset several hundreds of meters east of the summit; b) the local transtensive trend with N60° direction represented by a dextral strike-slip fault that links the cinder cones of São Mateus area, on the south coast of the island, to a series of dykes on the north-eastern coastline. This fault has been related to the rotation of the Nubian plate relative to the Eurasian (Marques et al., 2014), causing the observed offset of the N120° regional trend. The eruptive fissure that cross-cuts the summit crater also has N60° direction; and c) the Lomba de Fogo-São João (LFSJ) direct fault with N150° direction that crosses through Pico volcano and drove different magmas during the 1718 eruption (Zanon and Frezzotti, 2013). Another fault with the same direction of the LFSJ is represented by the Santo António fault on the northeast flank of the volcano. However, cinder cones along this fault show a smooth morphology and are partially buried by younger lavas, suggesting that this fault cannot be associated with recent magmatism. The area between these two N150° faults is devoid of cinder cones, which suggests that the strain produced by the tectonic stress field is limited.

3. Samples and methods

Twenty samples were collected from cinder cones and lava flows associated with the three tectonic systems intersecting Pico volcano (Fig. 1 and Table 1). Six lavas were sampled on the summit of the volcano, from the inner walls of the crater, the nested hornito, and the outer crater rim (a rheomorphic lava) (blue star in Fig. 1). The other samples (lavas and tephras) were collected along the flanks of the volcano (green stars in Fig. 1) from the topmost stratigraphic units, following the geological map of the island (Nunes, 1999). Table 1 summarises the most relevant information of the samples used in this study.

3.1. Whole-rock and mineral geochemistry

Major and trace element compositions of 15 rock samples were measured at Actlabs (Activation Laboratories, Canada) using a Perkin Elmer 9000 inductively coupled plasma-mass spectrometer (ICP-MS) and an Agilent 735 inductively coupled plasma-atomic emission spectrometer (ICP-AES). Alkaline dissolution with lithium metaborate/tetraborate followed by nitric acid was used on 1 g of rock powder before being fused in an induction furnace. The melt was poured into a solution of 5% nitric acid containing cadmium as an internal standard and stirred until complete dissolution. Resulting analytical precision is better than 5% for all major elements and 8% for most minor and trace elements (supplementary data). Sixteen international rock standards were used to calibrate the two methods. Whole-rock major and trace element compositional data are reported in Table 2.

Major element compositions of olivines and clinopyroxenes were measured at the University of Milan (Italy) using a JEOL JXA 8200 Superprobe equipped with five wavelength-dispersive spectrometers, an energy-dispersive detector and cathodoluminescence system. A spot size of 1 mm with a beam current of 5 nA was used throughout the measurements. Counting times were 30 s on the peak and 10 s on each background. Natural and synthetic minerals, used as standards, were calibrated within 2% at 2σ. Raw data were corrected applying a Phi–Rho–Z quantitative analysis program. The typical detection limit for each element is 0.01%. The relative errors are better than 6% for P_2O_5 and K_2O and better than 3% for all the other major elements.

3.2. Fluid inclusion microthermometry

Fluid inclusions (FI) were analysed in seven lava and five tephra samples. Approximately 1.5 kg of each sample was coarsely crushed and sieved to separate the largest crystal grain size present. For each sample 30-40 olivines (0.4-0.7 cm across) and clinopyroxenes (up to 1.2 cm in length) were thinned up to 80-100 μm and doubly polished. Microthermometry of FI was carried out on a Linkam MDSG600 heating-cooling stage, calibrated according to synthetic fluid inclusion standards of pure CO_2 and H_2O. Melting and homogenisation temperatures are reproducible to ±0.1°C with heating between 0.2–0.5°C/min.

Density values of the CO_2 fluid were calculated following equations 3.14 and 3.15 of Span and Wagener (1996). Isochores for a pure CO_2 fluid were calculated through the application of the equation of state of CO_2 of Sterner and Bodnar (1994), valid up to at least 2000°K and 10 GPa. For CO_2-H_2O inclusions (H_2O:CO_2 = 1:9), densities were calculated in accordance to the equation provided in Sterner and Bodnar (1991), after the application of the fluid density correction suggested by Hansteen and Klügel (2008). Isochores were calculated using the FLUIDS program (Bakker, 2003). Microthermometric data are shown in Table 3.

Densities of lava samples were measured through a MD 200s electronic densimeter and corrected for porosity. Density resolution is 1 kg·m^{-3}.

3.3. Radiocarbon and cosmogenic ^{3}He dating

Radiocarbon dating was performed on a paleosol rich in organic material, underlying a tephra deposit originated from the summit crater. The sample was collected on the southeastern upper flank of the volcano. The radiocarbon age was determined by Accelerator Mass Spectrometry (AMS) at Beta Analytic Radiocarbon Dating Laboratory (USA), after a pre-treatment with acid washes (HCl). Further information on the AMS method is available at the Beta Analytic website (www.radiocarbon.com). The reported age is expressed as radiocarbon years before present (BP) (present being AD 1950), using the international convention of a half-life of 5568 years. Age uncertainties are based on 1σ counting statistics. When calculated σ is lower than 30 years, it is conservatively rounded up to ±30 years BP.

In the absence of carbonised material associated with the emplacement of volcanic products, cosmogenic He exposure ages were determined on six pahoehoe lavas collected from well-preserved deltas along the coastline and from a fresh-looking cinder cone on the western upper flank of the volcano. From each site three fragments of lava were sampled after recording their bedding attitude (strike and dip). Clinopyroxene crystals were hand-picked under a binocular microscope from coarsely crushed samples and cleaned in distilled water. Weathered grains and with adhering volcanic glass were discarded. Crystals were separated in subsets for data replication.

The isotopic composition of magmatic He was determined on ~1 g of clinopyroxene by analysis of the gas released by *in vacuo* crushing using a hydraulic crusher (Stuart et al. 2003). Crushed clinopyroxene powders of grain size <125 mm were wrapped in aluminium foil and heated in a double-walled resistance furnace to 1800°C in order to extract the cosmogenic He. All samples were reheated at 1800°C to ensure total degassing. The active gases released by both extraction techniques were removed by sequential exposure to two SAES GP50 getters at 500°C for 20 minutes. The heavy noble gases were subsequently adsorbed onto activated charcoal cooled to -196°C using liquid nitrogen prior to the introduction in the mass spectrometer. A cold GP50 getter and N-cooled charcoal finger close to the mass spectrometer source were employed to minimise the partial pressure of residual gases during analysis. Helium isotope ratios and concentrations were determined using a *ThermoFisher* Helix-SFT mass spectrometer following procedures presented in Carracedo et al. (2019). ^{3}He and ^{4}He blanks for crushing and heating averaged $1{\cdot}10^{5}$ and $2{\cdot}10^{8}$ atoms, respectively. The reproducibility of standard He abundances during the period of analysis was ±1.1% for ^3He and ±0.5% for $^3He/^4He$. Cosmogenic He ages (Table 1) were determined using procedures described in Foeken et al. (2012) and are summarised here.

The concentration of cosmogenic He ($^3He_{cos}$) is calculated from:

$$^3He_{cos} = {^4He_{melt}} \times ({^3He/^4He_{melt}} - {^3He/^4He_{crush}})$$

where $^4He_{melt}$ and $^3He/^4He_{melt}$ are the He concentration and isotopic ratio of the melt steps, and $^3He/^4He_{crush}$ is the isotopic ratio of the magmatic He released by crush extraction. Age calculations have been computed using the CRONUScalc exposure age online calculator (http://web1.ittc.ku.edu:8888/1.0/). Details of scaling factors and production rates used are given in D'Amato et al. (2017).

3.4. Seismic data

Seismic data used in this study were acquired by the permanent monitoring network installed at Pico Island and operated by the Centro de Informação e Vigilância Sismovulcânica dos Açores (CIVISA). The seismic network comprises five short-period stations: three deployed around Pico volcano and one on each end of the island. The CIVISA database contains a total of 403 earthquakes recorded at Pico Island and offshore between January 2008 and December 2018.

Since the configuration of the seismic network changed over this period and in order to consider only high-quality data, we performed a selection of events, requiring that earthquakes were recorded in at least three stations and with root mean square of travel time residuals (RMS) of ≤0.3 s (using the standard seismic velocity model for the Azores region; Hirn et al., 1980; Senos et al., 1980). In total 335 seismic events were selected following the above criteria, while the remaining 68 events were excluded from this analysis. The high-quality events were relocated using the HYP program, a modified version of HYPOCENTER (Lienert and Havskov, 1995), integrated in the SEISAN 10.3 analysis software (Havskov and Ottemöller, 1999) and a five-layer 1D P-wave velocity model for Pico Island based on the model of Matias et al. (2007) for offshore Faial (Fig. 2).

The seismic velocity model assumes a layered structure and increasing P-wave velocity with depth. The upper layer (<3 km) corresponds to the island edifice made of basaltic lavas, which overlies the oceanic crust composed of mid-ocean ridge basaltic (MORB) lavas (3 to 8 km). The middle-lower oceanic crust (8 to 12.5 km) corresponds to intrusive gabbroic bodies, while the lower crust (12.5 to 17.5 km) is formed by ultramafic cumulates. In this model the MTZ was set at 17.5 km depth and separates the oceanic crust from the upper mantle rocks (c.f. Zanon and Frezzotti, 2013; Spieker et al., 2018).

4. Data description

4.1. Petrography and geochemistry

The petrographic and geochemical characteristics of the sampled rocks allow us to distinguish two types of magma erupted in the last 10 ka:

Type-A: porphyritic with >30 vol% crystal content, composed of clinopyroxene (Ø ≤25 mm) and olivine (Ø ≤1.5 mm) (Fig. 3a). Plagioclase is present only as microphenocrysts (Ø ≤0.6 mm). Lava texture is intergranular or intersertal. Clinopyroxene crystals are euhedral to subhedral. Megacrysts (up to 2.4 cm in length) always show patchy zoned texture, at least at the core, with a late-stage overgrowth with oscillatory zoning (Fig. 3b). Clinopyroxene composition is poorly variable (En_{40-46}, Fs_{5-9}, Wo_{37-39}). Olivine crystals are euhedral or rarely skeletal and their composition is between Fo_{78-86}. Plagioclase is euhedral or subhedral isolated crystals with rather homogeneous composition (An = 70 ±2.2). These lavas are basalts (SiO_2 = 46.5-48 wt%; Na_2O+K_2O = 3.25-4.0 wt%; Fig. 4) and represent the compositions emitted from lateral vents at low altitudes. However, the mineral assemblage and compositions of a tephra layer (high on the volcano ≥ 900 m a.s.l.) and a rheomorphic lava (close to the summit crater), both correlated with a lava fountain event of the summit, also fall within the range described above. Type-A lavas (and tephra layer) show no evidence, at both macro and microscale, of mixing/mingling of magmas with different compositions.

Type-B: porphyritic, with variable crystal content up to 35-40 vol% of euhedral plagioclase crystals with variable size (up to 1.8 cm), a few clinopyroxene crystals (Ø ≤2.2 mm) and rare olivine microphenocrysts (Ø = 0.25-0.45 mm) (Fig. 3c). Lava textures are intersertal. The mineral chemistry is similar to type-A lavas. Titanomagnetite is present as microphenocrysts and in the groundmass. Glomeroporphyritic aggregates of small plagioclases ±clinopyroxenes are common. These lavas are alkali basalts to trachybasalts (SiO_2 = 46.6-48.4 wt%; Na_2O+K_2O = 4.7-5.7 wt%; Fig. 4) and represent the compositions emitted from the summit of the volcano and sub-terminal vents.

The two types of magma are also evident from the variability of compatible vs. incompatible element contents. Most samples of both types fall on a straight line in the Zr/Sc vs. Sc diagram (Fig. 5a), where are also plotted the compositions of primitive melt inclusions sampled by olivines erupted at the Planalto da Achada fissure zone (Métrich et al., 2014). The variability of the melting conditions (i.e., melting degree and depth of melting) generates a straight line on a diagram where the ratio between the concentrations of a highly incompatible trace element, such as Rb, Th or Zr, over a moderately incompatible element, such as Sc, is compared with a highly incompatible element. Magma mixing processes would produce a curved line (Schiano et al., 2010).

The compositional variability of compatible trace elements of type-B magmas recalls that of the melt inclusions (Fig. 5b); i.e., low and constant element concentrations (i.e., Ni = 83 ±18 ppm; Co = 37 ±2 ppm; Cr = 32 ±17 ppm). Type-A magmas have higher and more variable compatible element concentrations compared to type-B magmas, due to the accumulation of mafic phases. Strontium behaves as an incompatible element as it increases from 467 ±55 ppm in type-A magmas to 635 ±57 ppm in type-B magmas (Fig. 5c). This suggests that plagioclase fractionation occurs only in limited cases. The frequent occurrence of small glomeroporphyritic aggregates (plagioclase ±clinopyroxene) may be related to late stage cotectic crystallization together with clinopyroxene at shallow depth during degassing of these magmas.

Mass-balance calculations using whole-rock compositions and the average composition of phenocrysts (Table 4) show that type-A magmas can be produced by adding 9.5-11.0% modal olivine (Mg# = 86%) and 17.5-28.5% modal clinopyroxene (Mg# = 85%) to the melt compositions trapped at the base of the crust below Planalto de Achada fissure zone, i.e. at or near the MTZ. The melt inclusions represent the silicate liquid assemblage available beneath the island prior to accumulation/fractionation processes (Métrich et al., 2014). Type-B magmas cannot be reproduced by simple fractional crystallisation of type-A magmas. It must involve a liquid composition stored at the MTZ and requires the fractionation of olivine (Mg# = 86%), clinopyroxene (Mg# = 89%), plagioclase (An = 66%), and a minimal accumulation of oxides, with -1.4%, -6%, -3% and +1.3% modal amounts, respectively (Fig. 6, Table 4).

4.2. Fluid inclusions

Fluid inclusions (FI) are common in olivine and occasional in clinopyroxene phenocrysts in type-A lavas. They were not found in clinopyroxene megacrysts. By contrast, they are rare or sporadic in olivines in type-B lavas and were not found in plagioclases and clinopyroxenes.

Inclusions are rounded or rarely elliptic with size ≤ 15-20 μm. At room temperature they are single phase (L) or may contain a vapour bubble (L+V). In rare cases inclusions are twocomponents and show two nested bubbles (L_1+V_1+L_2). These inclusions are frequent in large subhedral olivine phenocrysts, while they are rare in euhedral phenocrysts. Haloes of small FI (Ø <1 μm) surrounding a main inclusion cavity and/or short cracks radiating from a micro-cavity are frequent and reveal that events of partial density re-equilibration have occurred (Viti and Frezzotti, 2000; Viti and Frezzotti, 2001). Many silicate melt inclusions with variable size and crystallisation degree coexist with FI. These melt inclusions may contain a large CO_2-rich inclusion, which was also measured with the microthermometric stage. This suggests the contemporaneous trapping of fluid and melt within the same host.

Based on textural characteristics it is possible to distinguish two types of FI. The most abundant inclusions are trails of variable length and thickness, which line healed fractures, limit or cross cut grain boundaries. Inclusions rarely occur isolated or in small and spatially defined clusters, located both inside the grains and at boundaries. The interpretation of these textural characteristics and their utility for the understanding of the history of crystallisation of these magmas can be found in Zanon and Frezzotti (2013).

Inclusions frozen at < -75°C melt between -56.5 and -56.9°C confirming the pure CO_2 composition of the fluid. In large two-component inclusions, clathrate melting is detected starting from -11°C. The poor transparency of host crystals prevented the estimation of the H_2O/CO_2 ratio that was assumed to be 1/10, in accordance with Hansteen and Klügel (2008) and references therein. Final CO_2 homogenisation occurs either to the liquid (Th_L) or the vapour phase (Th_V). The range of Th_L varies between 24.7 and 31.1°C, corresponding to densities between 715 and 466 $kg{\cdot}m^{-3}$, while the recorded Th_V is only 31.0°C, corresponding to a density value of 461 $kg{\cdot}m^{-3}$. Table 3 reports the microthermometric data and integrates with data published by Zanon and Frezzotti (2013).

4.3. Density peaks interpretation

As shown by previous studies, the low magma ascent rates in the Azores prevent the formation of large melt-dominated reservoirs (i.e., Zanon and Frezzotti, 2013; Zanon, 2015b; Zanon and Pimentel, 2015; Zanon and Viveiros, 2019). Therefore, each erupted magma has followed a distinct ascent path that is recorded by the FI assemblage, for instance unimodal or polymodal fluid density distributions.

During magma ascent, inclusions may develop fluid over-pressure and decrepitate, forming small fractures radiating from the main cavity where fluid diffuses, thus reducing its pristine density. The re-crystallisation of the host crystals during ponding stages/ascent seals the fractures. This results from a single FI distribution where the inclusion with the highest fluid density, which does not show evidence of decrepitation, is a proxy for the entrapment conditions. A polymodal distribution formed by multiple events of decrepitation and/or fluid trapping is difficult to interpret. Therefore, only the comparison of FI distributions from samples representative of different magmas erupted on a short period can identify the various density peaks that represent important stratigraphic discontinuities at depth.

5. Results

5.1. Magma feeding system configuration

Figure 7 shows histograms of FI density distributions generated by eruptions occurring on the three tectonic systems intersecting the flanks of Pico volcano and on the summit crater. Data from the literature is also incorporated to increase consistency. The data distribution is polymodal (Fig. 7) and shows similar density peaks (marked by arrows in the histograms). Peaks represent fluid trapping/re-equilibration events related to limited stops during magma ascent. Relevant data calculated from FI are summarised in Table 5 as a function of the feeding system.

Fluid density was re-calculated for each peak, assuming 10 mol% H_2O content. Pressures estimates were obtained from isochore distribution in the P-T space at the trapping temperature of 1150°C (Zanon and Frezzotti, 2013). This value is similar to the 1165°C obtained as equilibrium temperature between the parental liquid (melt inclusion D5-b, Métrich et al., 2014) and $Fo_{85\%}$, at 500 MPa, using the model of Herzberg and O'Hara (2002). This temperature should therefore be considered as a good proxy for the eruptive temperature of basalts at Pico. Pressures were converted into depth using the stratigraphic scheme presented in Figure 2 and based upon the P-wave velocity model developed by Matias et al. (2007) for Faial offshore. This scheme considers a crustal thickness of ~18 km (Zanon and Frezzotti, 2013; Spieker et al., 2018).

The highest density values are similar in all systems (769-772 $kg{\cdot}m^{-3}$), except in the N60° system, and correspond to pressures of 489-501 MPa. Depths calculated from these pressures range from 17.3 to 17.7 km, close to the MTZ. Ponding at this depth was prolonged to assure the fractionation of primitive olivine (Fo_{87-89}) and fragments of fertile ultramafic lithologies. Carbonic fluids present in the lithosphere at this depth were trapped in crystallising olivines, forming early stage FI assemblages.

At shallower depth a common density peak at 740-748 $kg{\cdot}m^{-3}$ is evident in almost all histograms. These lithostatic pressures (459-470 MPa) correspond to depths of 16.3-16.7 km and coincide with a discontinuity in the mafic plutonic bodies at the base of the crust. These rocks and the rocks of the overlying layer should be compact and un-fractured, since fragments of these formations are only found in lavas emitted from the north vents of the 1718 eruption. They contain rounded gabbro fragments and the last recorded re-equilibration event occurred at a pressure of 419 MPa, which corresponds to a depth of 15.1 km (Zanon and Frezzotti, 2013).

Another common episode of FI re-equilibration in olivines (but also in clinopyroxenes, see Zanon and Frezzotti, 2013) occurred at lithostatic pressures between 329 and 400 MPa corresponding to depths of 12.1-14.5 km. Fractional crystallisation of clinopyroxene ±olivine formed clinopyroxenite bodies that are characterised by a bulk density of ~3100 kg·m^{-3} (measured in xenoliths with an electronic densimeter). Other ponding levels common to the three tectonic systems are found at lithostatic pressures ranging from 251 to264 MPa and from 206 to 216 MPa, corresponding to depths of 9.4-9.8 km and 7.7-8.1 km, respectively.

Magma ascent below the summit crater followed a different path with a prolonged ponding at a depth of 13.6 km, which allowed for the almost complete reset of high-density FI, and a reduced number of ponding steps at depths that do not coincide with those marked at the tectonic systems intersecting the volcano.

Except for the N120° system, magmas emitted from the other feeding systems record a further ponding stage marked by FI densities ranging from 345 to 435 kg·m^{-3}. This corresponds to lithostatic pressures within the range of 150-180 MPa (i.e., depths of 5.6-6.8 km).

5.2. Seismicity

The seismicity recorded by the CIVISA permanent monitoring network between 2008 and 2018 was characterised by frequent but discrete low magnitude ($M_L \leq 2.6$) volcano-tectonic earthquakes. The analysis of epicentre distribution (Fig. 8) shows that the seismicity is related to Pico volcano, with earthquakes scattered along the entire western part of the island and offshore, and a cluster of events located in the southern flank of the volcano, between the summit crater and the coastline. There was no seismicity associated with Planalto da Achada fissure zone during the period under analysis. The same pattern of seismicity recorded at Pico Island is reported in previous studies (Nunes, 1999; Gaspar et al., 2015). No seismic swarms were recorded and no systematic variation of earthquake activity with time was found for the period 2008-2018.

The depth of the relocated hypocentres range from 0 to 19.6 km (Fig. 8), with most of the earthquakes concentrated between 4 and 7 km beneath the south flank of Pico volcano. This cluster of hypocentres defines a seismogenic region of approximately 13 km^3. The microseismicity is concentrated roughly where the N150º and N60º tectonic systems intersect each other. The intersection of the fault systems originates structurally weak areas that facilitate the intrusion of dykes and sills into shallow depths where magma can be stored (Lourenço et al., 1998; Nunes et al., 2006).

6. Discussion

Merging the information obtained from petrology, geochemistry, and FI microthermometry with that from seismicity recorded by the permanent monitoring network, allows us to unravel the magma feeding system of Pico volcano, as shown in the cross-sections of Figure 9. Here we discuss the development of the magma feeding system during the Holocene and the role of the tectonic systems in the ascent of different magmas.

Recent volcanism (< 50 ka) such as that of Pico volcano can be dated by radiocarbon. However, this requires carbon, in the form of burned organic material associated with the emplacement of volcanic products. The availability of organic carbon on active volcanoes depends on climatic conditions and eruption frequency, and may not be available (Pimentel et al., 2016). In this study, in the absence of carbon, we have used cosmogenic ^3He dating to confirm the age of the recent volcanic activity at Pico. While the technique cannot compete with the accuracy of radiocarbon, the results show that the cosmogenic ^3He method corroborates that the recent basaltic volcanism from Pico volcano is Holocene in age. Our new cosmogenic ^3He

ages are in agreement with the radiocarbon ages associated with the geological map (Nunes, 1999).

All magmas ascending through the mantle below Pico volcano in the last 10 ka gathered in a main storage area at a depth of 17.3-17.7 km, where they may pond indefinitely and crystallise. This marks the most important ponding level for all magmas ascending through the deep lithosphere and corresponds to the present-day MTZ, where magmas reach neutral buoyancy conditions (Cushman et al., 2004; Schwartz et al., 2004; Nicolosi et al., 2006; Civile et al., 2008). This level marks the transition from mantle rocks to ultramafic cumulates, with a small density difference but significantly different petrography (for details on the petrographic features of these rocks see Zanon and Frezzotti, 2013; Métrich et al., 2014). This minimum difference in density has a small effect on the seismic velocity (see Fig. 2). Data interpretation from receiver functions in the islands closer to the Mid-Atlantic Ridge, identified this major discontinuity at ~16 km depth (Spieker et al., 2018), while previous seismic velocity models set it at 12.5 km (Matias et al., 2007).

Above the MTZ, every magma that ascended through the three tectonic systems intersecting the volcano (especially N120° and N60°) followed independent ascent paths, arresting frequently for a limited period. These short ponding periods occurred when magmas reached a buoyancy threshold after ongoing crystallisation and consequent formation of a crystal mush composed of clinopyroxene fractionated from the melt. The FI found in large antecrysts of clinopyroxene are in fact re-equilibrated (Zanon and Frezzotti, 2013), suggesting a different residence time of those antecrysts in the crystal mush from the olivine of the magma that destabilised the mush. Important stacked sills and associated crystal mushes at 12.1-14.5 km depth may be responsible for the seismic anomaly which geophysicists interpreted as the Moho discontinuity in previous works on the Azores (see Matias et al., 2007) and also on other oceanic islands (i.e., Gallart et al., 1999; Pim et al., 2008; Martinez-Arevalo et al., 2013; Fontaine et al., 2015). In our interpretation this discontinuity represents the "geophysical Moho", i.e., the crust/mantle boundary before the formation of Pico Island. If we subtract the thickness of the submerged and emerged island edifice (~1,300 and 2,351 m, respectively) we obtain a thickness of oceanic crust of 8.3-10.9 km, which is in agreement with previous estimates of the crustal thickness (e.g., White et al., 1982). All these elements show that the crust/mantle boundary and the deepest magma ponding levels deepened with time. We propose that this deepening is caused by underplating. Underplated magmas cannot ascend directly to the surface because of the absence of open ascent paths. These magmas, therefore, remain accumulated at the base of the crust (i.e., at the MTZ) where they crystallise. If we assume that the construction of Pico Island started in the last 500 ka (the oldest subaerial rock is dated at 270 ±150 ka; Demande et al., 1982), we estimate a growth rate of 1 cm/yr beneath the island by underplating.

From field and petrographic constraints we recognise a sequence of ultramafic cumulate layers of variable composition (dunites, olivine-clinopyroxenites, clinopyroxenites) and intrusive gabbroic bodies. All these rocks contain carbonic FI assemblages (c.f., Zanon and Frezzotti, 2013) with densities comparable to the highest values found in our samples, which shows they are at or nearby the present-day MTZ. Furthermore, due to voluminous underplating, magma ponding levels in the area between the present-day MTZ and the geophysical Moho are surrounded by a well-developed crystal mush prone to consolidate to form stiff cumulates. When the accumulation of tectonic stress activates deep faults a rapid tapping of magmas located at the MTZ is allowed. Their rapid ascent through these crystal mush zones mobilises the crystal mushes, forming the typical clinopyroxene and olivine-rich type-A magmas.

It is important to underline that type-A magmas from all tectonic systems maintained their high content of mafic crystals afloat in the melt and preserved the signature of the many events of partial re-equilibration in FI. This latter element shows that the ascent path followed by these magmas was almost isochoric, as also showed by the low volumes of fractionated mineral phases. Overall, this suggests a very rapid magma ascent from the MTZ to the surface.

Magma ponding at shallower depths, i.e. in the old oceanic crust (made up by layered intrusions and submarine MORB lavas), is not prolonged enough to allow for significant crystal fractionation and formation of crystal mushes. A shallow magma ponding level is present in the upper crust at a depth of 5.6-6.8 km, which is associated with the emission of magmas through the N150° and N60° systems and the summit crater. Comparing the depth obtained from FI data with that of the cluster of earthquakes recorded beneath the south flank of the volcano, it can be observed that there is an overlap. In this area, the hypocentres are concentrated at depths between 4 and 7 km. This last ponding level can be interpreted as a region with a dense network of dykes and sills filled with magmas currently evolving towards type-B. This network of intrusions seems to be the source of the frequent microseismicity and might be related to the early stages of formation of a more complex shallow reservoir eccentric to the summit, located at the intersection of the N150° and N60° fault systems. The existence of a shallow network of magma intrusions is also supported by gravimetric data obtained for Pico Island, which does not reveal any gravity anomalous body beneath Pico volcano that could be interpreted as a large magma reservoir (Nunes et al., 2006). A shallow reservoir, in a more mature stage, is however showed by seismic tomography and petrological data beneath Caldeira central volcano (in the nearby Faial Island) at a similar depth of 3-7 km (Dias et al., 2007; Zanon et al., 2013).

Magmas emitted from the summit crater in the last 5 ka were almost exclusively of type-B. At the same time, frequent eruptions of type-A magmas occurred on the flanks from the N120° and N60° systems, through lateral vents at low altitudes. The only exception is a small but violent explosive event of type-A magma (represented by samples Pic66s and Pic89) that occurred at the summit approximately 740 ^{14}C years BP. The ascent of this magma from 13.7 km was fast enough to allow the transport of an exceptional mafic crystal cargo. There is no evidence of interaction with type-B magmas, suggesting that this magma ascended either through a different pathway coaxial with the summit, or dragged upwards after a period of prolonged type-B magma effusions which emptied the upper part of the feeder system, allowing a fast decompression of type-A magma at depth.

The regional and the local tectonics play a major role in the activation of the different magma feeder systems of Pico through time. The shift from fissure volcanism (N120° regional transtensive system) to the formation of the central volcano is related to the activation of the local N60° transtensive system. This led to the ascent of magma through a more centralised and well-established system of dykes. The N60° system was repeatedly activated during the last 5 ka. It was responsible for lateral eruptions involving type-A magmas, the migration of the summit towards the NE, and the eruptive fissure that crosses the summit crater. Most probably, the explosive event of type-A magma at the summit 740 years BP was also promoted by this system, taking into consideration the petrographic characteristics, mineral assemblage, and ponding depths similar to the other magmas erupted along the N60° system. The activity of the N150° system (LFSJ direct fault) seems to be limited to the last 5 ka and was probably responsible for the formation of the eccentric shallow magma ponding level at the intersection with the N60° system, where type-B magma formed after ponding for some time. This fault is apparently related to the incipient development of a graben on the northern flank of the volcano, together with the Santo António fault system.

The basic configuration of the magma feeder system of Pico volcano is similar to many other oceanic volcanoes where multiple stacked sills are present at a wide range of depths in the crust, and spanning the MTZ (Brandsdóttir et al., 1997; Hansteen et al., 1998; MacIennan et al., 2001;

Schwarz et al., 2004; Klügel et al., 2005; Stroncik et al., 2009; Neave and Putirka, 2017; Boudoire et al., 2019; MacIennan, 2019; White et al., 2019), and are separated by well-developed crystal mushes. Frequent recharges of these systems fluidise the mushes, entraining crystals in the ascending melt with a process of chaotic mixing. This explains the coexistence of antecrysts and phenocrysts with different genetic histories (Ruprecht and Bachmann, 2010; Cashman, and Blundy, 2013).

At oceanic volcanoes magma ascent occurs mostly along fissure zones, whose origin is still debated as in the case of the Canary Islands and Hawaii volcanoes (e.g., Dieterich, 1988; Carracedo, 1994; Anguita and Hernán, 2000; Munn et al., 2006; Geyer and Martì, 2010; Denlinger and Morgan, 2014). At the Canary Islands lithospheric faults with regional importance activate during late stage volcanism to feed scattered eruptions (Fernández et al., 2006). However, the role played by the interplay of regional (deep) and local tectonics to induce changes in the stress field and to control magma ascent is not exclusive of Pico volcano, as it is also observed at Piton de La Fournaise, on La Reunion Island (Michon et al., 2015; Boudoire et al., 2019) and at some Icelandic volcanoes (Opheim and Gudmundsson, 1989; Gudmundsson, 2000; Tibaldi et al., 2008). It is however important to remark that these examples are not strictly associated with extensional geodynamic settings such as that of the Azores, where the interplay of stresses related to regional fissure systems and local transtensive faults is truly determinant for magma ascent.

7. Conclusions

This multidisciplinary study integrating petrological, geochemical, and fluid-inclusion studies with seismic monitoring data allowed us to better understand how the magma feeding system works beneath Pico volcano (Azores) and how it is associated with the activation of three tectonic systems. Two petrographically and geochemically distinct magmas were emitted at the same time in the last 10 ka. The emission of olivine- and clinopyroxene-rich magmas (type-A) occurred mostly along the flanks of the volcano, while plagioclase dominated magmas (type-B) erupted at the summit crater during the last 5 ka. Type-A magmas ascended directly and rapidly from the Moho Transition Zone at a depth of 17.3-17.7 km, while type-B magmas ascended from a shallow magma ponding level located at 5.6-6.8 km depth. This last ponding level seems to be related to the frequent microseismicity recorded by the permanent monitoring network beneath the southern flank of the volcano at depths between 4 and 7 km, which might be associated with the early stages of development of a more complex magma reservoir.

The information obtained in this work provides a clearer image of the magma feeding system of a young basaltic oceanic volcano, in particular the depths where magmas pond and their ascent paths. The replication of this multidisciplinary approach to other poorly monitored oceanic volcanoes could allow for a significant improvement of the knowledge of their eruptive behaviour and can have important implications on the mitigation of volcanic risk related to a possible future forthcoming unrest.

Acknowledgements

The Portuguese Fundação para a Ciência e Tecnologia (FCT) through project MARES (PTDC/GEO-FIQ/1088/2014) supported the analytical work and grants of GM and MA. Free access to the summit of Pico volcano during field surveys in 2016, 2017 and 2018 has been provided by the Parque Natural do Pico. The Centro de Informação e Vigilância Sismovulcânica dos Açores (CIVISA) is acknowledged for providing the seismic data. Authors are grateful to the staff of the Centro de Aquisição de Dados of CIVISA and also to S. Oliveira for the help with the seismic database. A. Risplendente and S. Poli of the "Ardito Desio" University of Milan (Italy) are acknowledged for providing help during microprobe analyses. Finally, two anonymous reviewers are acknowledged for the useful comments that significantly improved the quality of this manuscript.

References

Anguita, F., Hernán, F., 2000. The Canary Islands origin: a unifying model. Journal of Volcanology and Geothermal Research 103, 1-26.

Bachmann, O., Bergantz, G.W., 2008. Rhyolites and their source mushes across tectonic settings. Journal of Petrology 49, 2277-2285.

Bakker, R.J., 2003. Package FLUIDS 1. Computer programs for analysis of fluid inclusion data and for modelling bulk fluid properties. Chemical Geology 194, 3-23.

Baxter, P.J., Gresham, A., 1997. Deaths and injuries in the eruption of Galeras Volcano, Colombia, 14 January 1993. Journal of Volcanology and Geothermal Research 77, 325-338.

Beier, C., Haase, K.M., Turner, S.P., 2012. Conditions of melting beneath the Azores. Lithos 144-145, 1-11.

Boudoire, G., Brugier, Y.-A., Di Muro, A., Wörner, G., Arienzo, I., Métrich, N., Zanon, V., Braukmüller, N., Kronz, A., Le Moigne, Y., Michon, L., 2019. Eruptive activity on the western flank of Piton de la Fournaise (La Réunion Island, Indian Ocean): insights on magma transfer, storage and evolution at an oceanic volcanic island. Journal of Petrology in press, doi: 10.1093/petrology/egz045.

Brandsdóttir, B., Menke, W., Einarsson, P., White, R.S., Staples, R.K., 1997. Färoe- Iceland ridge experiment 2. Crustal structure of the Krafla central volcano. Journal of Geophysical Research: Solid Earth 102, 7867-7886.

Carracedo, J.C., 1994. The Canary Islands: an example of structural control on the growth of large oceanic-island volcanoes. Journal of Volcanology and Geothermal Research 60, 225-241.

Carracedo, Á., Rodés, A., Smellie, J., Stuart, F.M., 2019. Episodic erosion in West Antarctica inferred from cosmogenic ^{3}He and ^{10}Be in olivine from Mount Hampton. Geomorphology 327, 438-445.

Carrara, A., Burgisser, A., Bergantz, G.W., 2019. Lubrication effects on magmatic mush dynamics. Journal of Volcanology and Geothermal Research 380, 19-30.

Cashman, K., Blundy, J., 2013. Petrological cannibalism: the chemical and textural consequences of incremental magma body growth. Contributions to Mineralogy and Petrology 166, 703-729.

Civile, D., Lodolo, E., Tortorici, L., Lanzafame, G., Brancolini, G., 2008. Relationships between magmatism and tectonics in a continental rift: the Pantelleria Island region (Sicily Channel, Italy). Marine Geology 251, 32-46.

Claude-Ivanaj, C., Joron, J.L., Allègre, C.J., 2001. ^{238}U–^{230}Th–^{226}Ra fractionation in historical lavas from the Azores: long-lived source heterogeneity vs. metasomatism fingerprints. Chemical Geology 176, 295-310.

Costa, A.C.G., Marques, F.O., Hildenbrand, A., Sibrant, A.L.R., Catita, C.M.S., 2014. Large-scale catastrophic flank collapses in a steep volcanic ridge: the Pico–Faial Ridge, Azores Triple Junction. Journal of Volcanology and Geothermal Research 272, 111-125.

Costa, A.C.G., Hildenbrand, A., Marques, F.O., Sibrant, A.L.R., Santos de Campos, A., 2015. Catastrophic flank collapses and slumping in Pico Island during the last 130 kyr (Pico-Faial ridge, Azores Triple Junction). Journal of Volcanology and Geothermal Research 302, 33-46.

Corsaro, R.A., Miraglia, L., 2005. Dynamics of 2004–2005 Mt. Etna effusive eruption as inferred from petrologic monitoring. Geophysical Research Letters 32, L13302.

Cushman, B., Sinton, J.M., Ito, G., Dixon, J.E., 2004. Glass compositions, plume- ridge interaction, and hydrous melting along the Galápagos Spreading Center, 90.5° W to 98° W. Geochemistry, Geophysics, Geosystems 5, Q08E17.

D'Amato, D., Pace, B., Di Nicola, L., Stuart, F.M., Visini, F., Azzaro, R., Branca, S., Barfod, D.N., 2017. Holocene slip rate variability along the Pernicana fault system (Mt. Etna, Italy): Evidence from offset lava flow. Geological Society of America Bulletin 129, 304-317.

Demande, J., Fabriol, R., Gérard, A., Iundt, F., 1982. Prospection géothermique des Iles de Faial et Pico (Açores). Rapport d'avancement. Bureau de Recherches Géologiques et Minières, Orléans, France, p. 20.

Denlinger, R.P., Morgan, J.K., 2014. Instability of Hawaiian volcanoes. In: Poland, M.P., Takahashi, T.J., Landowski, C.M. (Eds.), Characteristics of Hawaiian volcanoes. U.S. Geological Survey Professional Papers 1801, pp. 149-176.

Dias, N.A., Matias, L., Lourenço, N., Madeira, J., Carrilho, F., Gaspar, J.L., 2007. Crustal seismic velocity structure near Faial and Pico islands (Azores), from local earthquake tomography. Tectonophysics 445, 301-317.

Dieterich, J.H., 1988. Growth and persistence of Hawaiian volcanic rift zones. Journal of Geophysical Research 93, 4258–4270.

Fernández, C., Casillas, R., García Navarro, E., Gutiérrez, M., Camacho, M.A., Ahijado, A., 2006. Miocene rifting of Fuerteventura (Canary Islands). Tectonics 25, TC6005.

Foeken, J.P.T., Stuart, F.M., Mark, D.F., 2012. Long-term low latitude ^{3}He production rate determined from a 126 ka basalt from Fogo, Cape Verdes. Earth and Planetary Science Letters 359-360, 14-25.

Fontaine, F.R., Barruol, G., Tkalčić, H., Wölbern, I., Rümpker, G., Bodin, T., Haugmard, M., 2015. Crustal and uppermost mantle structure variation beneath La Réunion hotspot track. Geophysical Journal International 203, 107-126.

Gallart, J., Driad, L., Charvis, P., Sapin, M., Hirn, A., Diaz, J., Voogd, B., Sachpazi, M., 1999. Perturbation to the lithosphere along the hotspot track of La Réunion from an offshore-onshore seismic transect. Journal of Geophysical Research: Solid Earth 104, 2895-2908.

Gaspar, J.L., Queiroz, G., Ferreira, T., Medeiros, A.R., Goulart, C., Medeiros, J., 2015. Earthquakes and volcanic eruptions in the Azores region: geodynamic implications from major historical events and instrumental seismicity. in: Gaspar, J.L., Guest, J.E., Duncan, A.M., Barriga, F.J.A.S., Chester, D.K. (Eds.), Volcanic Geology of São Miguel Island (Azores Archipelago). The Geological Society of London, Memoirs 44, pp. 33-49.

Gente, P., Dyment, J., Maia, M., Goslin, J., 2003. Interaction between the Mid-Atlantic Ridge and the Azores hot spot during the last 85 Myr: Emplacement and rifting of the hot spot-derived plateaus. Geochemistry, Geophysics, Geosystems 4, 8514-8537.

Georgen, J.E., Sankar, R.D., 2010. Effects of ridge geometry on mantle dynamics in an oceanic triple junction region: Implications for the Azores Plateau. Earth and Planetary Science Letters 298, 23-34.

Geyer, A., Martí, J., 2010. The distribution of basaltic volcanism on Tenerife, Canary Islands: Implications on the origin and dynamics of the rift systems. Tectonophysics 483(3-4), 310-326.

Gudmundsson, A., 2000. Dynamics of volcanic systems in Iceland: example of tectonism and volcanism at juxtaposed hot spot and mid-ocean ridge systems. Annual Review of Earth and Planetary Sciences 28, 107-140.

Hansteen, T.H., Klügel, A., Schmincke, H.-U., 1998. Multi-stage magma ascent beneath the Canary Islands: evidence from fluid inclusions. Contributions to Mineralogy and Petrology 132, 48-64.

Hansteen, T.H., Klügel, A., 2008. Fluid inclusion thermobarometry as a tracer for magmatic processes, in: Putirka, K., Tepley, F. (Eds.), Reviews in Mineralogy and Geochemistry. Mineralogical Society of America 69, pp. 143-177.

Havskov J, Ottemöller L., 1999. SeisAn earthquake analysis software. Seismological Research Letters 70, 532-534.

Herzberg, C., O'Hara, M.J., 2002. Plume-associated ultramafic magmas of Phanerozoic age. Journal of Petrology 43, 1857-1883.

Hildreth, W., Wilson, C.J.N., 2007. Compositional zoning of the Bishop Tuff. Journal of Petrology 48, 951-999.

Hirn, A., Haessler, H., Hoangtrong, P., Wittlinger, G., Mendes-Victor, L.A., 1980. Aftershock sequence of the January 1st, 1980, earthquake and present-day tectonics in the Azores. Geophysical Research Letters 7, 501-504.

Huang, H.-H., Lin, F.-C., Schmandt, B., Farrell, J., Smith, R.B., Tsai, V.C., 2015. The Yellowstone magmatic system from the mantle plume to the upper crust. Science 348, 773-776.

Kiser, E., Palomeras, I., Levander, A., Zelt, C., Harder, S., Schmandt, B., Hansen, S.L., Creager, K., Ulberg, C., 2016. Magma reservoirs from the upper crust to the Moho inferred from high-resolution Vp and Vs models beneath Mount St. Helens, Washington State, US. Geology 44, 411-414.

Klügel, A., Hansteen, T.H., Galipp, K., 2005. Magma storage and underplating beneath Cumbre Vieja volcano, La Palma (Canary Islands). Earth and Planetary Science Letters 236, 211-226.

Lees, J.M., 2007. Seismic tomography of magmatic systems. Journal of Volcanology and Geothermal Research 167, 37-56.

Lienert, B.R., Havskov, J., 1995. A computer program for locating earthquakes both locally and globally. Seismological Research Letters 66, 26-36.

Lourenço, N.L.J.F., Miranda, J.M., Luis, J.F., Ribeiro, A., Victor, L.M., Madeira, J., Needham, H.D., 1998. Morpho-tectonic analysis of the Azores Volcanic Plateau from a new bathymetric compilation of the area. Marine Geophysical Researches 20, 141-156.

Maclennan, J., McKenzie, D., Gronvöld, K., Slater, L., 2001. Crustal accretion under northern Iceland. Earth and Planetary Science Letters 191, 295-310.

Maclennan, J., 2019. Mafic tiers and transient mushes: evidence from Iceland. Philosophical Transactions of the Royal Society A 377(2139), 20180021.

Madeira, J., Brum da Silveira, A., 2003. Active tectonics and first paleoseismological results in Faial, Pico and S. Jorge Islands (Azores, Portugal). Annals of Geophysics 46, 733-761.

Marques, F.O., Catalão, J.C., DeMets, C., Costa, A.C.G., Hildenbrand, A., 2013. GPS and tectonic evidence for a diffuse plate boundary at the Azores Triple Junction. Earth and Planetary Science Letters 381, 177-187.

Marques, F.O., Catalão, J., Hildenbrand, A., Costa, A.C.G., Dias, N.A., 2014. The 1998 Faial earthquake, Azores: Evidence for a transform fault associated with the Nubia–Eurasia plate boundary? Tectonophysics 633, 115-125.

Martinez-Arevalo, C., de Lis Mancilla, F., Helffrich, G., Garcia, A., 2013. Seismic evidence of a regional sublithospheric low velocity layer beneath the Canary Islands. Tectonophysics 608, 586-599.

Matias, L., Dias, N.A., Morais, I., Vales, D., Carrilho, F., Madeira, J., Gaspar, J.L., Senos, L., Silveira, A.B., 2007. The 9^{th} of July 1998 Faial Island (Azores, North Atlantic) seismic sequence. Journal of Seismology 11, 275-298.

Métrich, N., Zanon, V., Créon, L., Hildenbrand, A., Moreira, M., Marques, F.O., 2014. Is the "Azores hotspot" a wetspot? Insights from geochemistry of fluid and melt inclusions in olivines of Pico basalts. Journal of Petrology 55, 377-393.

Michon, L., Ferrazzini, V., Di Muro, A., Villeneuve, N., Famin, V., 2015. Rift zones and magma plumbing system of Piton de la Fournaise volcano: How do they differ from Hawaii and Etna? Journal of Volcanolology and Geothermal Research 303, 112-129.

Miranda, J.M., Mendes Victor, L.A., Simões, J.Z., Luis, J.F., Matias, L., Shimamura, H., Shiobara, H., Nemoto, H., Mochizuki, H., Hirn, A., Lépine, J.C., 1998. Tectonic setting of the Azores plateau deduced from a OBS survey. Marine Geophysical Researches 20, 171-182.

Miranda, J.M., Luis, J.F., Lourenço, N., Goslin, J., 2014. Distributed deformation close to the Azores Triple "Point". Marine Geology 355, 27-35.

Münn, S., Walter, T.R., Klügel, A., 2006. Gravitational spreading controls rift zones and flank instability on El Hierro, Canary Islands. Geological Magazine 143, 257–268.

Neave, D.A., Putirka, K.D., 2017. A new clinopyroxene-liquid barometer, and implications for magma storage pressures under Icelandic rift zones. American Mineralogist 102, 777-794.

Nicolosi, I., Speranza, F., Chiappini, M., 2006. Ultrafast oceanic spreading of the Marsili Basin, southern Tyrrhenian Sea: Evidence from magnetic anomaly analysis. Geology 34, 717-720.

Nunes, J.C., 1999. A actividade vulcânica na ilha de Pico do Plistocénico Superior ao Holocénico: mecanismo eruptivo e hazard vulcânico. Departamento de Geociências, Universidade dos Açores, Ponta Delgada, p. 357.

Nunes, J.C., Camacho, A., França, Z., Montesinos, F.G., Alves, M., Vieira, R., Velez, E., Ortiz, E., 2006. Gravity anomalies and crustal signature of volcano-tectonic structures of Pico Island (Azores). Journal of Volcanology and Geothermal Research 156, 55-70.

Opheim, J. A., Gudmundsson, A., 1989. Formation and geometry of fractures, and related volcanism, of the Krafla fissure swarm, northeast Iceland. Geological Society of America Bulletin 101, 1608-1622.

Pim, J., Peirce, C., Watts, A.B., Grevemeyer, I., Krabbenhöft, A., 2008. Crustal structure and origin of the Cape Verde Rise. Earth and Planetary Science Letters 272, 422-428.

Pimentel, A., Pacheco, J., Self, S., 2015. The ∼1000-years BP explosive eruption of Caldeira Volcano (Faial, Azores): the first stage of incremental caldera formation. Bulletin of Volcanology 77, 42.

Pimentel, A., Zanon, V., De Groot, L.V., Hipólito, A., Di Chiara, A., Self, S., 2016. Stress-induced comenditic trachyte effusion triggered by trachybasalt intrusion: multidisciplinary study of the AD 1761 eruption at Terceira Island (Azores). Bulletin of Volcanology 78, 22.

Queiroz, G., Gaspar, J.L., Guest, J.E., Gomes, A., Almeida, M.H., 2015. Eruptive history and evolution of Sete Cidades Volcano, São Miguel Island, Azores, in: Gaspar, J.L., Guest, J.E., Duncan, A.M., Barriga, F.J.A.S., Chester, D.K. (Eds.), Volcanic Geology of São Miguel Island (Azores Archipelago). The Geological Society of London, Memoirs 44, pp. 87-104.

Ruprecht, P., Bachmann, O., 2010. Pre-eruptive reheating during magma mixing at Quizapu volcano and the implications for the explosiveness of silicic arc volcanoes. Geology, 38, 919-922.

Sano, Y., Kagoshima, T., Takahata, N., Nishio, Y., Roulleau, E., Pinti, D.L., Fischer, T.P., 2015. Ten-year helium anomaly prior to the 2014 Mt Ontake eruption. Scientific Reports 5, 13069.

Schiano, P., Monzier, M., Eissen, J-P., Martin, H., Koga, K.T. 2010. Simple mixing as the major control of the evolution of volcanic suites in the Ecuadorian Andes. Contributions to Mineralogy and Petrology 160(2), 297-312.

Schwarz, S., Klügel, A., Wohlgemuth-Ueberwasser, C., 2004. Melt extraction pathways and stagnation depths beneath the Madeira and Desertas rift zones (NE Atlantic) inferred from barometric studies. Contributions to Mineralogy and Petrology 147, 228-240.

Senos, M.L., Nunes, J.C., Moreira, V.S., 1980. Estudos da estrutura da crosta e manto superior nos Açores. Instituto Nacional de Meteorologia e Geofísica, Lisboa.

Silva, P.F., Henry, B., Marques, F.O., Hildenbrand, A., Lopes, A., Madureira, P., Madeira, J., Nunes, J.C., Roxerová, Z., 2018. Volcano-tectonic evolution of a linear volcanic ridge (Pico-Faial Ridge, Azores Triple Junction) assessed by paleomagnetic studies. Journal of Volcanology and Geothermal Research 352, 78-91.

Span, R., Wagner, W., 1996. A new equation of state for carbon dioxide covering the fluid region from the triple point temperature to 1100 K at pressures up to 800 MPa. Journal of Physical and Chemical Reference Data 25, 1509-1596.

Sparks, R.S.J., 2003. Forecasting volcanic eruptions. Earth and Planetary Science Letters 210, 1-15.

Sparks, R.S.J., Biggs, J., Neuberg, J.W., 2012. Monitoring volcanoes. Science 335, 1310-1311.

Sparks, R.S.J., Annen, C., Blundy, J.D., Cashman, K.V., Rust, A.C., Jackson, M.D., 2019. Formation and dynamics of magma reservoirs. Philosophical Transaction of the Royal Society of London A 377, 20180019.

Spieker, K., Rondenay, S., Ramalho, R., Thomas, C., Helffrich, G., 2018. Constraints on the structure of the crust and lithosphere beneath the Azores Islands from teleseismic receiver functions. Geophysical Journal International 213, 824-835.

Sterner, S.M., Bodnar, R.J., 1991. Synthetic fluid inclusions; X, Experimental determination of P-V-T-X properties in the CO_2 -H_2O system to 6 kb and 700 degrees C. American Journal of Science 291, 1-54.

Sterner, S.M., Pitzer, K.S., 1994. An equation of state for carbon dioxide valid from zero to extreme pressures. Contributions to Mineralogy and Petrology 117, 362-374.

Stroncik, N.A., Klügel, A., Hansteen, T.H., 2009. The magmatic plumbing system beneath El Hierro (Canary Islands): constraints from phenocrysts and naturally quenched basaltic glasses in submarine rocks. Contributions to Mineralogy and Petrology 157, 593-607.

Stuart, F.M., Lass-Evans, S., Fitton, J.G. and Ellam, R.M., 2003. High $^3He/^4He$ ratios in picritic basalts from Baffin Island and the role of a mixed reservoir in mantle plumes. Nature 424 (6944), 57-59.

Tibaldi, A., Vezzoli, L., Pasquaré, F. A., Rust, D., 2008. Strike-slip fault tectonics and the emplacement of sheet–laccolith systems: the Thverfell case study (SW Iceland). Journal of Structural Geology 30, 274-290.

Trippanera, D., Porreca, M., Ruch, J., Pimentel, A., Acocella, V., Pacheco, J.M., Salvatore, M., 2014. Relationships between tectonics and magmatism in a transtensive/transform setting: An example from Faial Island (Azores, Portugal). Geological Society of America Bulletin 126, 164-181.

Turner, S., Hawkesworth, C., Rogers, N., King, P., 1997. U-Th isotope disequilibria and ocean island basalt generation in the Azores. Chemical Geology 139, 145-164.

Viti, C., Frezzotti, M.-L., 2000. Re-equilibration of glass and CO_2 inclusions in xenolith olivine: A TEM study. American Mineralogist 85, 1390-1396.

Viti, C., Frezzotti, M.-L., 2001. Transmission electron microscopy applied to fluid inclusion investigations. Lithos 55, 125-138.

Vogt, P.R., Jung, W.Y., 2004. The Terceira Rift as hyper-slow, hotspot-dominated oblique spreading axis: a comparison with other slow-spreading plate boundaries. Earth and Planetary Science Letters 218, 77-90.

Wager, L., Brown, G., Wadsworth, W., 1960. Types of igneous cumulates. Journal of Petrology 1, 73-85.

White, R.S., McKenzie, D., O'Nions, R.K., 1992. Oceanic crustal thickness from seismic measurements and rare earth element inversions. Journal of Geophysical Research: Solid Earth 97(B13), 19683-19715.

White, R.S., Edmonds, M., Maclennan, J., Greenfield, T., Agustsdottir, T., 2019. Melt movement through the Icelandic crust. Philosophical Transactions of the Royal Society of London A 377, 20180010.

Zanon, V., Kueppers, U., Pacheco, J. M., Cruz, I., 2013. Volcanism from fissure zones and the Caldeira central volcano of Faial Island, Azores archipelago: geochemical processes in multiple feeding systems. Geological Magazine 150, 536-555.

Zanon, V., Frezzotti, M.L., 2013. Magma storage and ascent conditions beneath Pico and Faial islands (Azores Islands). A study on fluid inclusions. Geochemistry, Geophysics, Geosystems 14, 3494-3514.

Zanon, V., 2015a. The magmatism of the Azores Islands, in: Gaspar, J.L., Guest, J.E., Duncan, A.M., Barriga, F.J.A.S., Chester, D.K. (Eds.), Volcanic Geology of São Miguel Island (Azores Archipelago). The Geological Society of London, Memoirs 44, pp. 51-64.

Zanon, V., 2015b. Conditions for mafic magma storage beneath fissure zones at oceanic islands. The case of São Miguel island (Azores archipelago), in: Caricchi, L., Blundy, J.D. (Eds.), Chemical, Physical and Temporal Evolution of Magmatic Systems. The Geological Society of London, Special Publications 422, pp. 85-104.

Zanon, V., Pimentel, A., 2015. Spatio-temporal variations of magma storage and ascent conditions in an extensional tectonic setting. The case of the Terceira Island, Azores (Portugal). American Mineralogist 100, 795-805.

Zanon, V., Viveiros, F., 2019. A multi-methodological re-evaluation of the volcanic events during the 1580 CE and 1808 eruptions at São Jorge Island (Azores Archipelago, Portugal). Journal of Volcanology and Geothermal Research 373, 51-67.

Figure captions

Figure 1. Digital elevation model of Pico Island showing the major tectonic systems (simplified from Madeira and Brum da Silveira, 2003) and sampling locations. Green stars mark the collection sites of new lava and tephra samples. Blue stars mark the collection sites of lavas inside the summit collapse crater. Yellow stars show the sampling sites of lavas studied by Zanon and Frezzotti (2013) and also considered in this study. White triangles mark the vents of the historical eruptions of Pico volcano and the light-blue triangle the vent of the historical

eruption of Planalto da Achada fissure zone. Inset a) shows the bathymetric map of the Azores region (Lourenço et al., 1998), superimposed on the main geostructural features from Marques et al. (2014).

Figure 2. 1D P-wave velocity model and petrological interpretation for Pico Island based on the model of Matias et al. (2007) for the Faial offshore.

Figure 3. Main petrographic characteristics of Pico rocks. Typical features of type-A rocks: a) large clinopyroxene and olivine phenocrysts are frequent in many rocks and are well-visible at hand specimen scale; and b) detail of the patchy zoning in clinopyroxene. c) Typical type-B rocks show an abundant presence of plagioclases and a reduced presence of mafic minerals.

Figure 4. Total alkali–silica (TAS) diagram of the new samples distinguished according to magma type. The yellow area shows selected literature data of Pico (Turner et al., 1997; Claude-Ivanaj et al., 2001; Beier et al., 2012; Zanon and Frezzotti, 2013).

Figure 5. Variability of representative trace elements in study rocks, compared with primitive silicate melt inclusions from the Planalto da Achada fissure zone. a) The effect of partial melting is responsible for the large variability of Zr (and other highly incompatible elements) in silicate melt inclusions as also discussed by Métrich et al. (2014). b) The variability of Ni versus Zr is used to mark the effect of fractionation/accumulation of olivine, due to its high compatibility in this mineral. c) Sr is used to monitor the plagioclase behaviour.

Figure 6. Graphical result of mass balance calculation applied to our dataset, using the variability of the CaO/Al_2O_3 and FeO/MgO ratios as a monitor. While the first ratio varies as a function of plagioclase and clinopyroxene fractionation/accumulation, the second accounts for olivine and clinopyroxene fractionation/accumulation. The parental melt for all calculations is a set of poorly evolved silicate melt in olivines erupted by basalts of the Planalto da Achada fissure zone (Métrich et al., 2014).

Figure 7. Histograms of fluid inclusion density distribution in the olivines hosted by magmas erupted at the three tectonic systems and the summit crater. The highest density value recorded by these fluid inclusions is 738 $kg{\cdot}m^{-3}$ and represents the deepest ponding level at the Moho Transition Zone, marked with a grey dashed line (see also the discussion in Zanon and Frezzotti, 2013). Blue colour marks data related to events of early and/or late-stage fluid inclusions formation. Red arrows show the highest value of density recorded by these populations in each diagram and mark a ponding level. Decrepitated fluid inclusions are reported in grey-striped columns. Peaks of re-equilibration are marked by a grey arrow.

Figure 8. Epicentres and hypocentres of the relocated earthquakes recorded between 2008 and 2018 by the permanent monitoring network operated by the Centro de Informação e Vigilância Sismovulcânica dos Açores (CIVISA) at Pico Island. Map view and N-S and E-W cross-sections are shown. A cluster of earthquakes is seen in the southern flank of the volcano in the map view, at depths between 4 and 7 km in the cross-sections.

Figure 9. Conceptual model of the magma feeding system of Pico volcano resulting from the merging of data from fluid inclusions microthermometry and local seismicity. Inset shows the

traces of the profiles, following the faults on the volcano. The geophysical Moho and the present-day Moho Transition Zone (MTZ) are marked by dashed lines. The seismogenic region beneath the volcano is represented by a pattern of circles. Thin blue lines show the depths suitable for sheet intrusion formation within the cumulate layers beneath the N120° and N150° systems. The formation of these sheeted bodies beneath the N60° system is reduced. The grey area around the storage areas in the cumulitic bodies indicates a mature crystal mush made of clinopyroxenes.

Table captions

Table 1. Sample location, type and age.

[1] Pic66s and Pic89 are the distal tephra fallout and rheomorphiclava, respectively, emitted during a lava fountain event of the summit.

[2] Charcoal ^{14}C age, this study.

[3] Cosmogenic ^{3}He age, this study.

[4] Charcoal ^{14}C age from Nunes (1999).

[5] Age estimate based on the geological map (Nunes, 1999).

Table 2. Whole-rock major and trace element compositional data.

Table 3. Microthermometry data.

New samples are reported in bold, while samples studied by Zanon and Frezzotti (2013) are reported in italics for comparison.

Table 4. Mass-balance calculations.

* Data from Métrich et al. (2014)

Mg# = Mg/(Mg+Fe^{+2}) modal

An = Ca/(Ca+Na+K) modal

Table 5. Fluid inclusion density database for Pico volcano.

Samples studied by Zanon and Frezzotti (2013) are here reported in blue and bold for comparison. The highest density values are from inclusions without any visible evidence of decrepitation. Therefore, the distribution of these inclusions does not have an associated error. Density peak values are aligned across the samples to better evidence the presence of significant discontinuities at depth.

Figure 1
Click here to download high resolution image

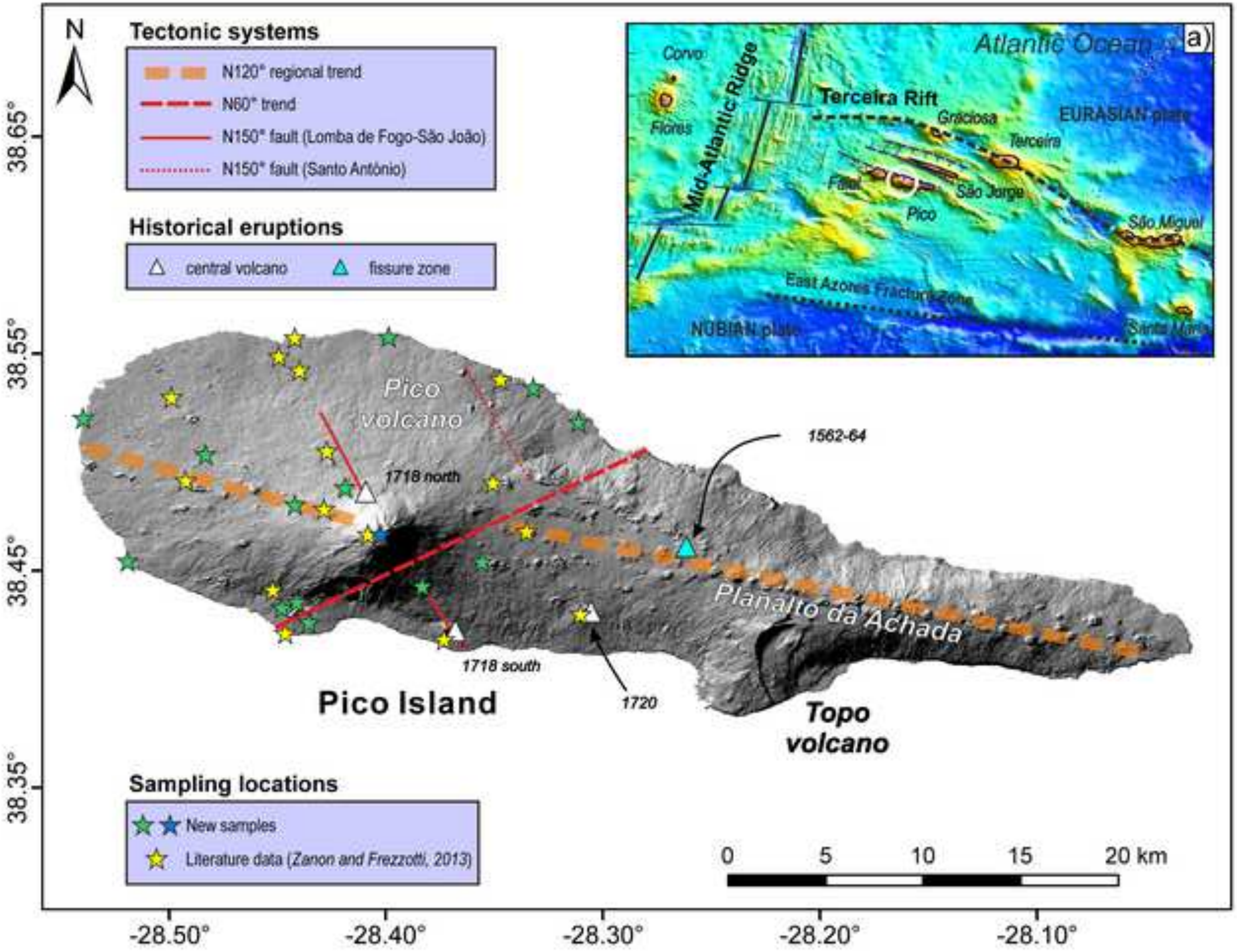

Figure 2
Click here to download high resolution image

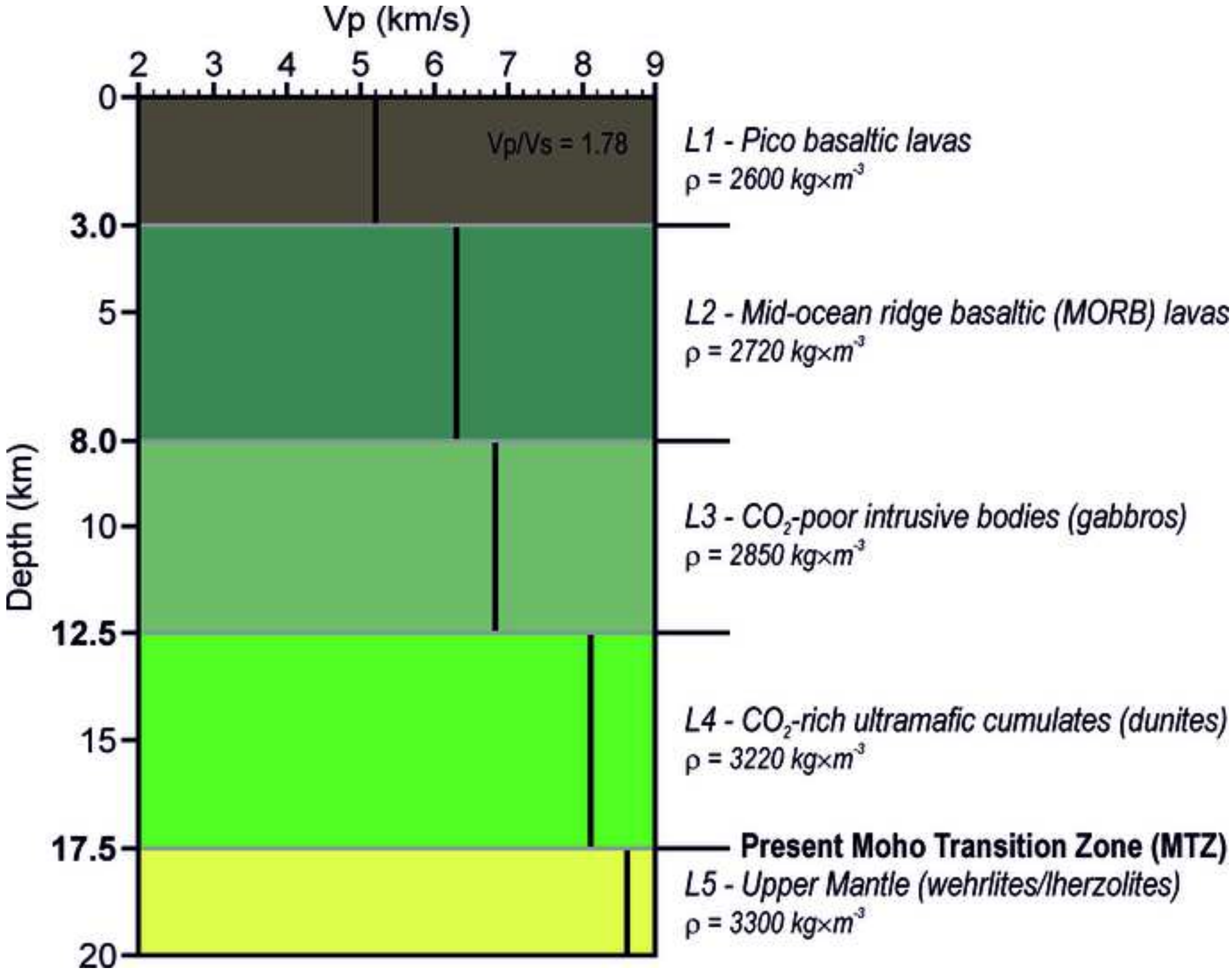

Figure 3
Click here to download high resolution image

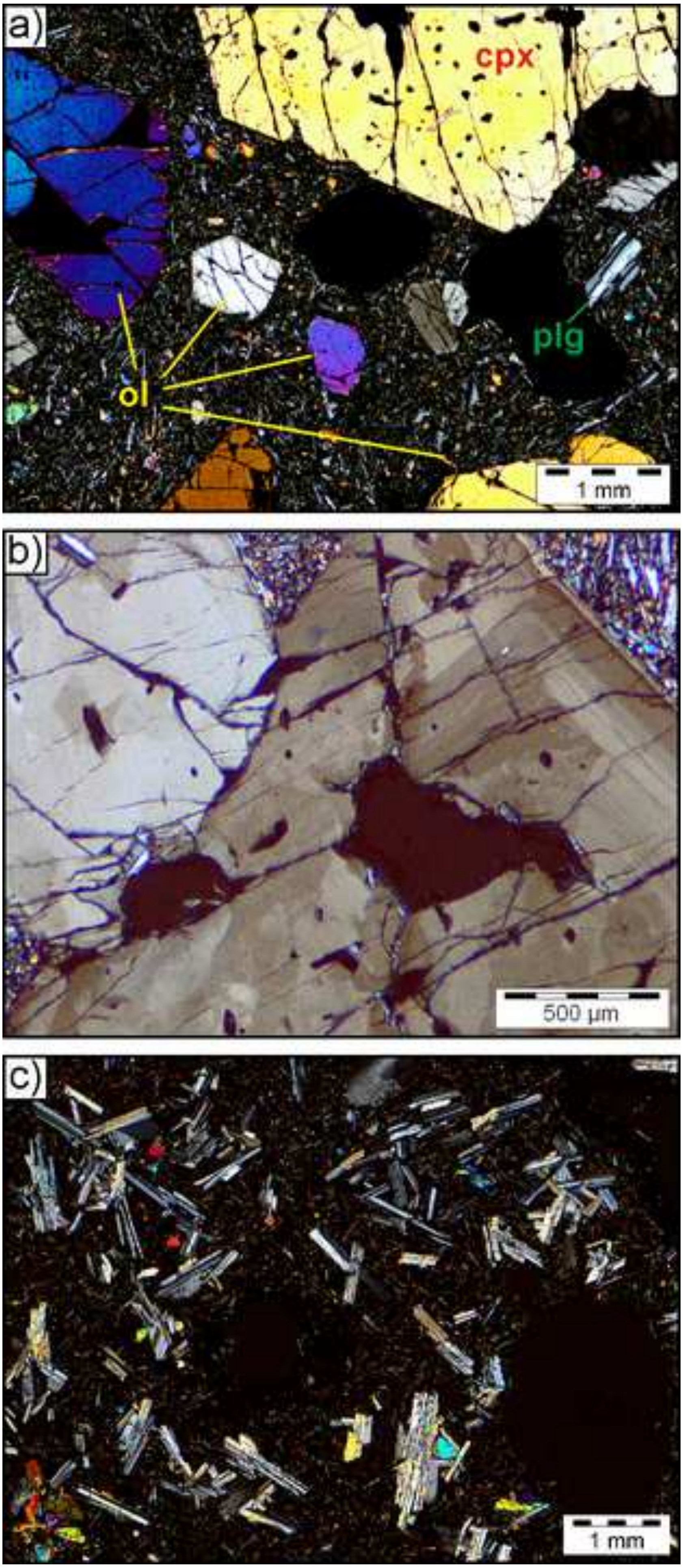

Figure 4
Click here to download high resolution image

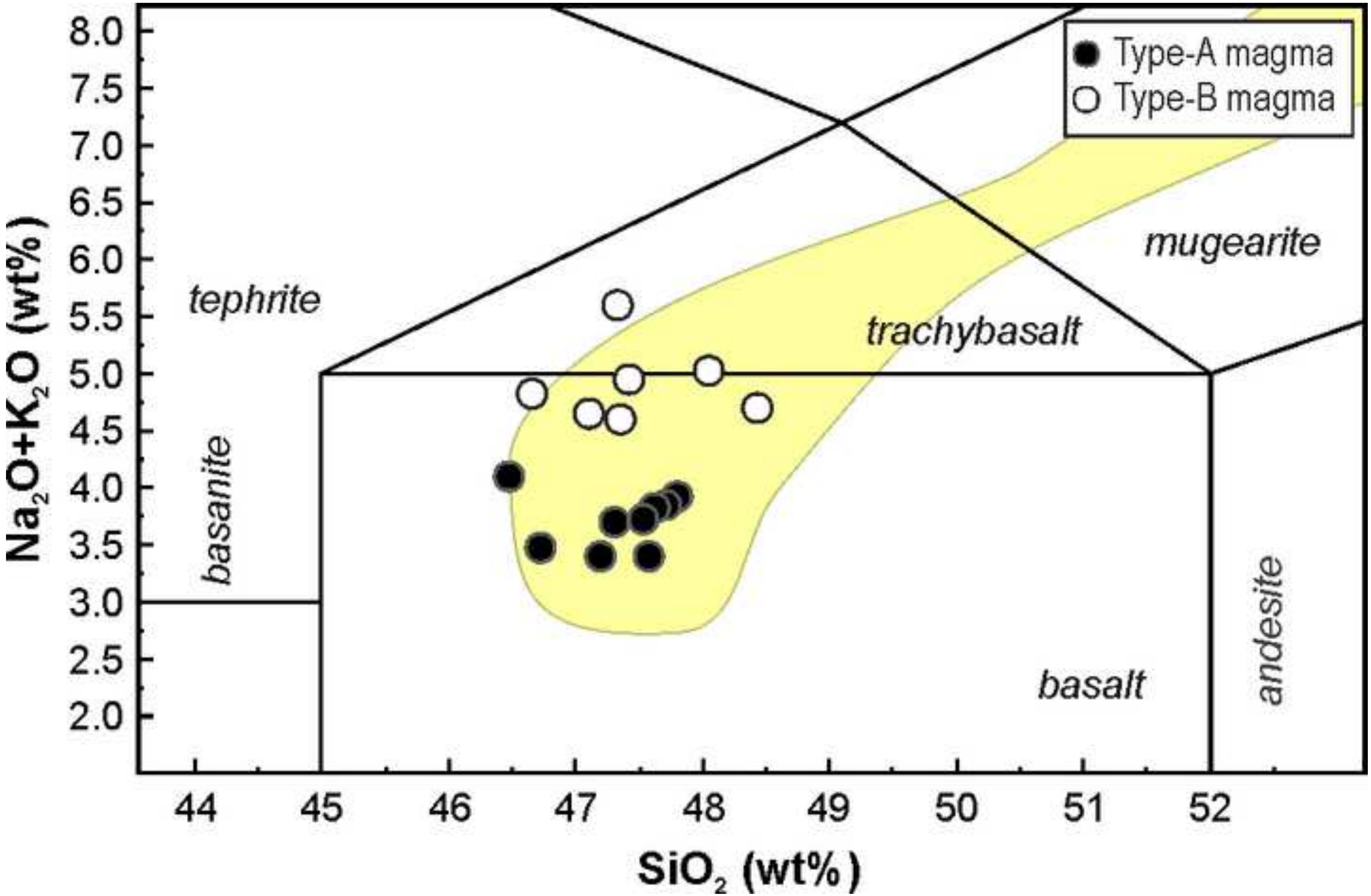

Figure 5
Click here to download high resolution image

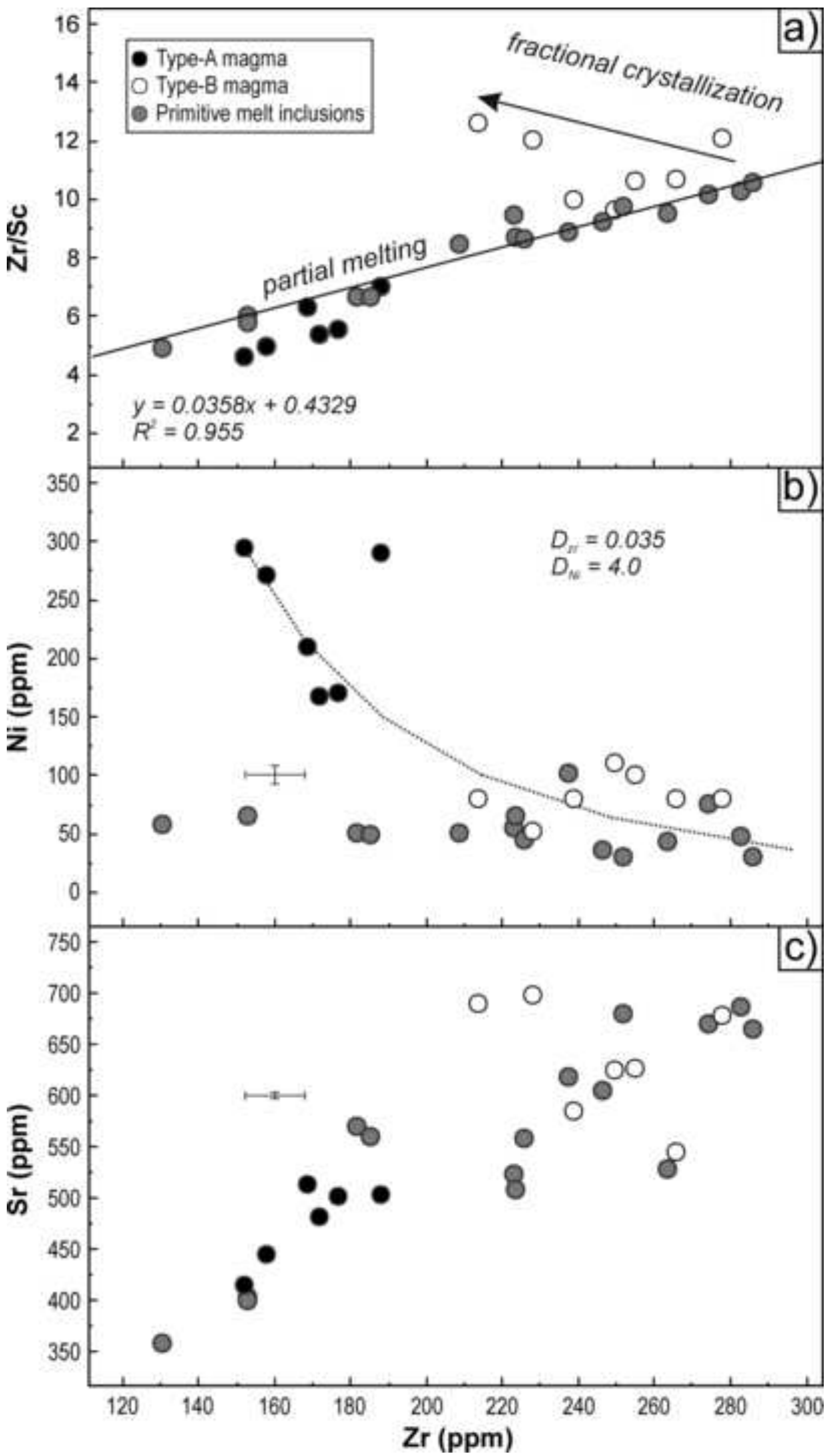

Figure 6

Click here to download high resolution image

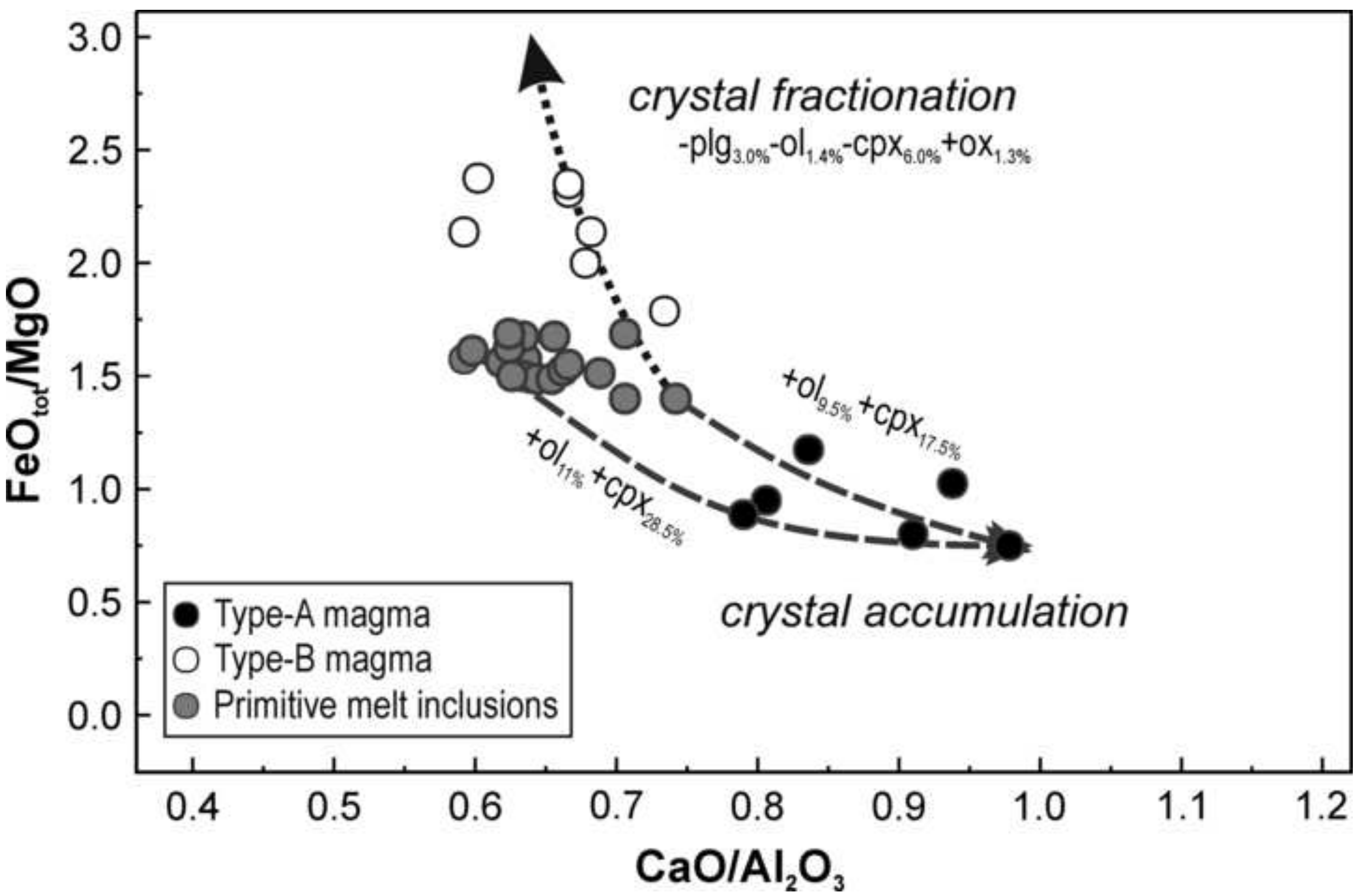

Figure 7
Click here to download high resolution image

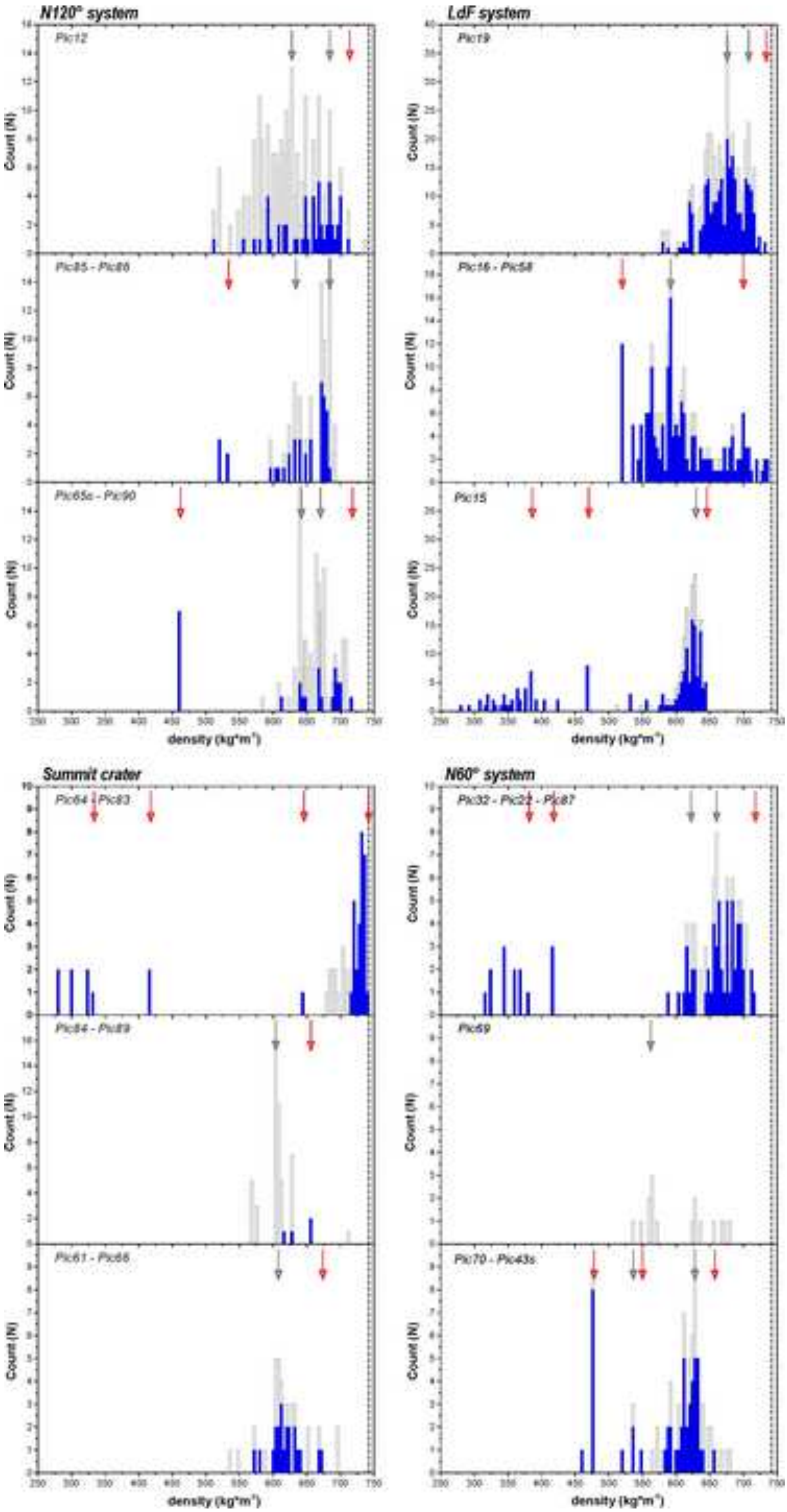

Figure 7b

Click here to download high resolution image

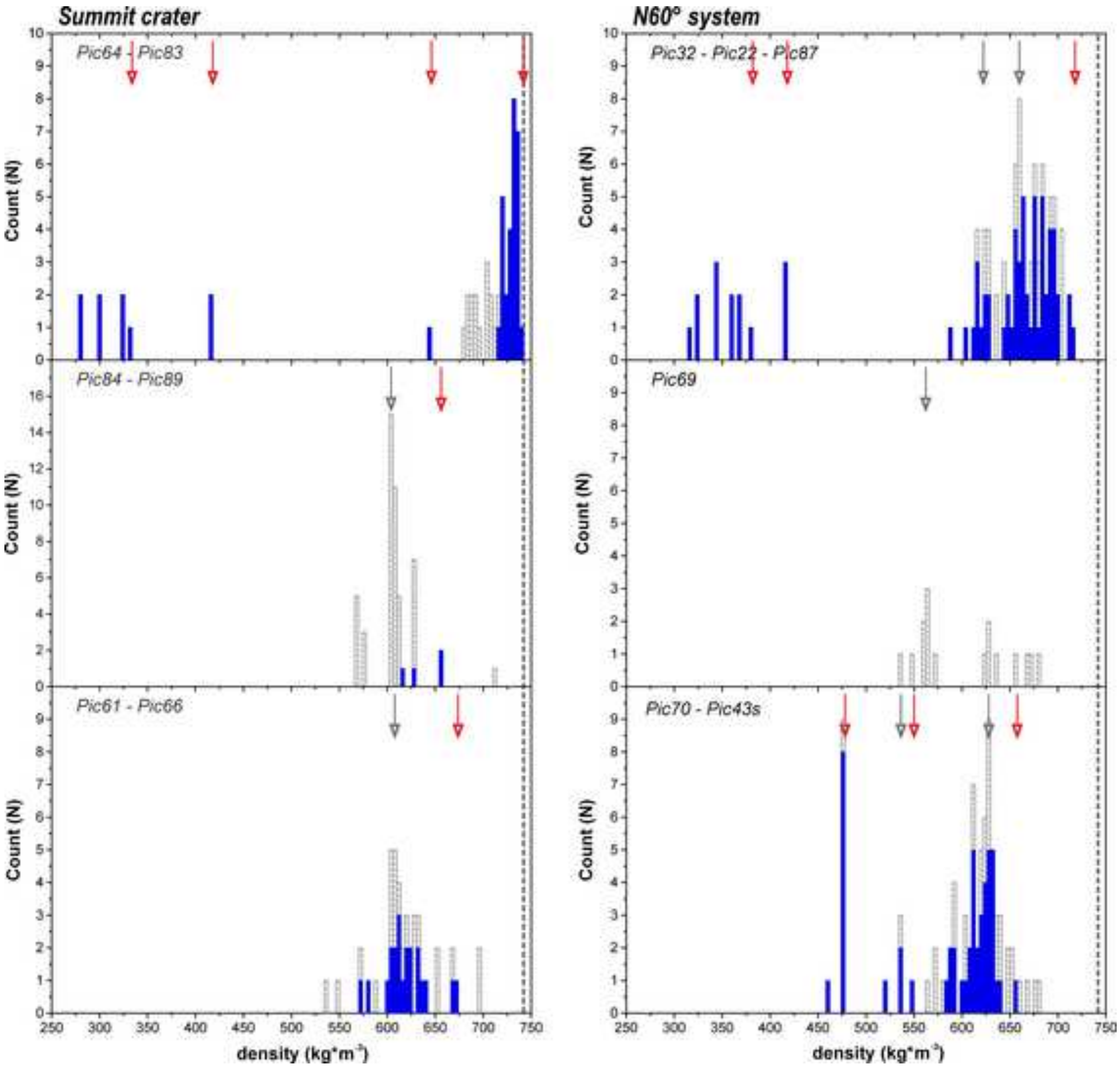

Figure 8
Click here to download high resolution image

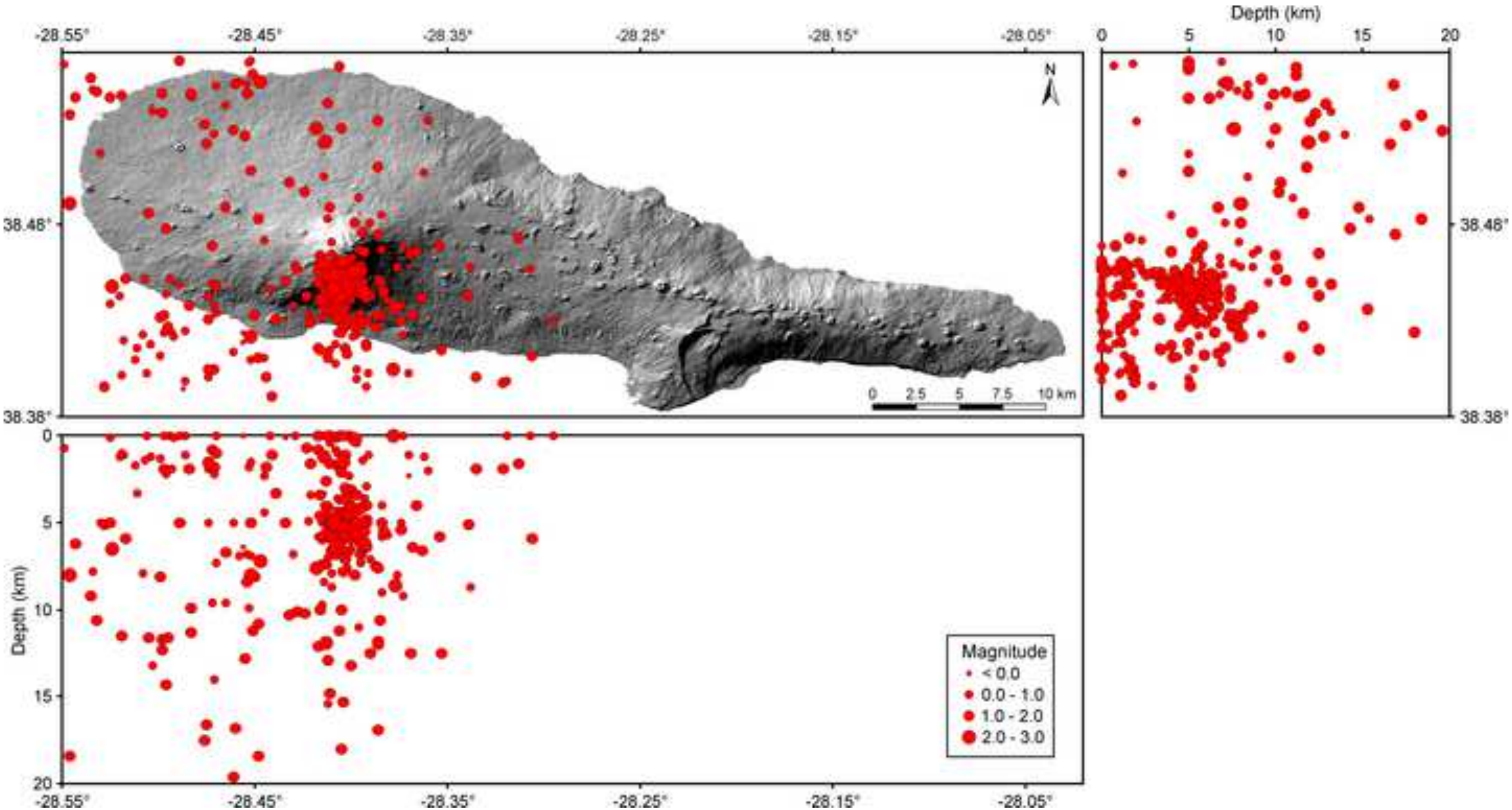

Figure 9
Click here to download high resolution image

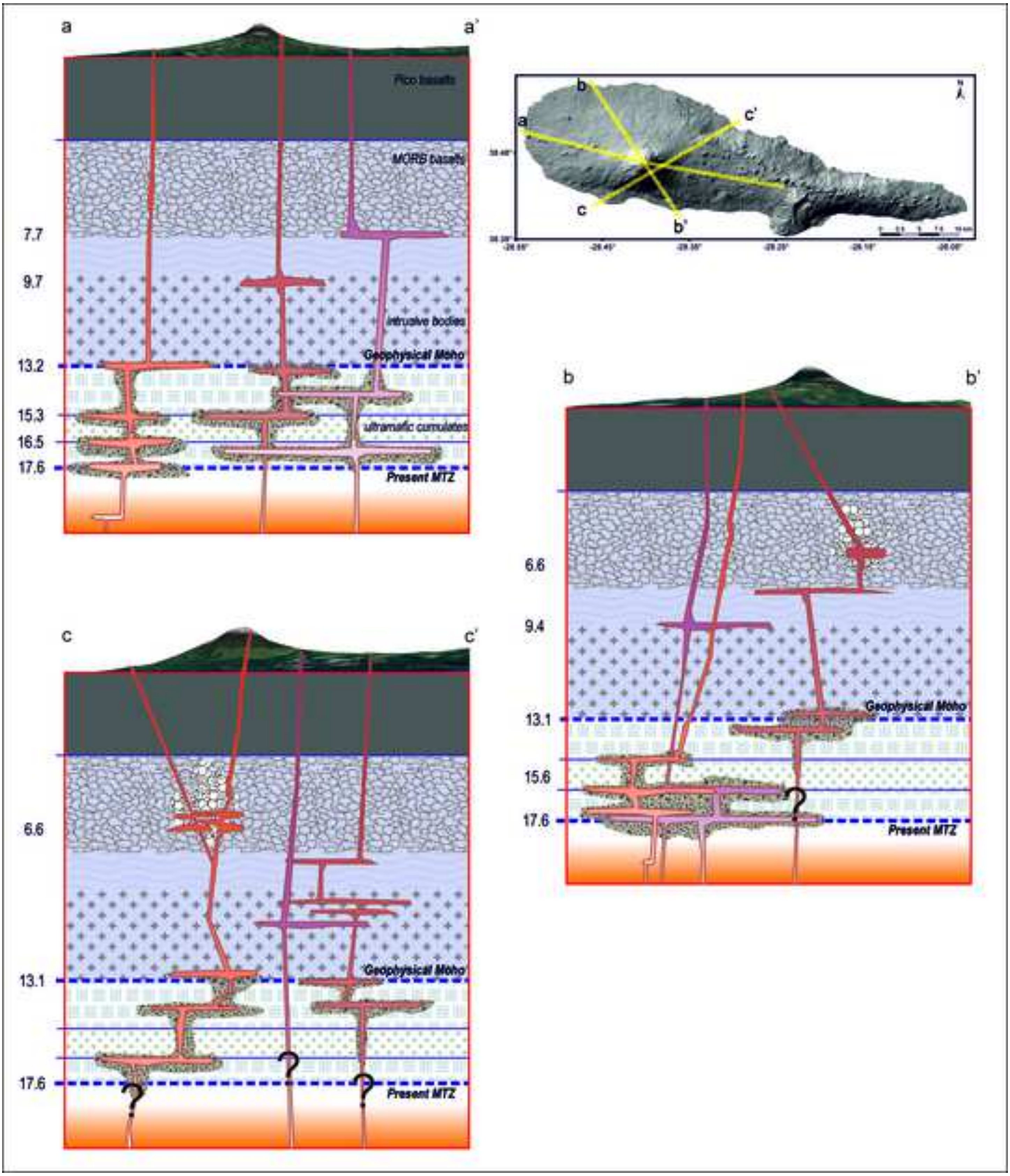

Table 1

Click here to download Table: Table 1 - sample list AP.docx

Table 1. ~~-~~**Sample location, type and age**

Sample~~Name~~ L~~l~~ocation	Latitude~~Long. (E)~~ Longitude ~~Lat. (N)~~	Material~~Type and m~~ Magma type	Age (ka)	Eruptive system	Mineral assemblage
Pic43 *Pico de Urze*	38.454039° ~~382112 E~~ -28.351073° ~~4257058 N~~	lava type A	0.62 ± 0.006[2]	N60°	cpx+ol
Pic45	38.476745° ~~382669 E~~ -28.345111° ~~4259570 N~~	lava type A	0.5-1[5]	N120°	ol+cpx
Pic46 *Cabeço das cabras*	38.475390° ~~375863 E~~ -28.423107° ~~4259522 N~~	lava type A	1.5-5[5]	N120°	cpx+ol
Pic65s	38.489580° ~~372859 E~~ -28.457829° ~~4261144 N~~	tephra type A	1.5-5[5]	N120°	cpx+ol+plg
Pic65	38.469488° ~~377549 E~~ -28.403665° ~~4258841 N~~	lava type B	1.4 ± 0.007[4]	summit crater	plg+ol+cpx
Pic66s[1]	38.443327° ~~378955 E~~ -28.387047° ~~4255916 N~~	tephra type A	0.74 ± 0.003[2]	summit crater	cpx+ol
Pic66	38.469485° ~~377529 E~~ -28.403894° ~~4258841 N~~	lava type B	1-1.5[5]	summit crater	plg+ol+cpx
Pic67	38.467111° ~~377627 E~~ -28.402725° ~~4258576 N~~	lava type B	1-1.5[5]	summit crater	plg
Pic68	38.467396° ~~377667 E~~ -28.402272° ~~4258607 N~~	tephra type B	1-1.5[5]	summit crater	plg+ol
Pic69	38.466526° ~~377697 E~~ -28.401911°	lava type B	1-1.5[5]	summit crater	plg+ol

	~~4258510 N~~				
Pic70	38.466622° ~~377741 E~~ - 28.401409° ~~4258520 N~~	lava type B	1-1.5[5]	summit crater	plg+ol
Pic69s *S. Mateus*	38.432052° ~~374873 E~~ - 28.433597° ~~4254727 N~~	tephra type A	1-1.5[5]	N60°	cpx+ol
Pic70s *S. Mateus II*	38.431970° ~~374162 E~~ - 28.441741° ~~4254729 N~~	tephra type A	1-1.5[5]	N60°	cpx+ol
Pic83	38.466750° ~~382097 E~~ - 28.351482° ~~4258469 N~~	lava type A	5.3 ± 2.4[1]	summit crater	ol+cpx
Pic84	38.558001° ~~378373 E~~ - 28.395928° ~~4268653 N~~	lava type A	8.8 ± 4.3[1]	summit crater	cpx+ol
Pic85	38.517950° ~~365802 E~~ - 28.539346° ~~4264408 N~~	lava type A	2.5 ± 1.0[1]	N120°	cpx+ol+plg
Pic86	38.447704° ~~368503 E~~ - 28.506901° ~~4256566 N~~	lava type A	9.3 ± 3.9[1]	N120°	ol+cpx
Pic87 *S. Mateus*	38.423261° ~~375663 E~~ - 28.424374° ~~4253739 N~~	lava type A	1-1.5[5]	N60°	cpx+ol
Pic89[1]	38.465289° ~~377740 E~~ - 28.401394° ~~4258372 N~~	lava type A	0.74 ± 0.003[2] 0.97 ± 0.71[1]	summit crater	cpx+ol
Pic90	38.474569° ~~374691 E~~ - 28.436526° ~~4259449 N~~	lava type A	1-1.5[5]	N120°	cpx+ol+plg

[1] Pic66s and Pic89 are the distal tephra fallout and rheomorphic~~agglutinated~~ lava, respectively, ~~produced~~ emitted during a lava fountain ~~an~~ event of the summit ~~lava fountain~~.
[2] Charcoal ^{14}C age, this study.
[3] Cosmogenic ^{3}He age, this study.
[4] Charcoal ^{14}C age from Nunes (1999).
[5] Age estimate based on the geological map (Nunes, 1999)~~field constraints~~.

Table 2
Click here to download Table: Table 2 - whole rock.docx

Table 2. Whole-rock data

	Pic83	Pic84	Pic85	Pic86	Pic87	Pic90	Pic43	Pic45	Pic46	Pic70	Pic65	Pic66	Pic67	Pic68	Pic69
SiO_2	47.03	47.02	46.82	47.11	46.77	46.78	47.41	46.31	47.33	47.86	46.37	46.19	46.51	45.93	46.91
TiO_2	2.32	2.35	3.31	2.69	2.01	2.35	2.20	2.32	1.96	3.11	3.28	3.20	3.57	3.57	2.89
Al_2O_3	13.67	13.17	16.78	12.57	11.38	12.25	12.03	13.12	10.78	16.12	15.84	15.10	15.44	16.26	17.21
FeO_{tot}	9.74	10.00	11.28	10.08	10.10	10.02	9.79	10.02	9.91	10.47	10.93	11.00	11.62	11.39	10.11
MnO	0.17	0.17	0.17	0.18	0.16	0.17	0.16	0.17	0.16	0.17	0.18	0.18	0.19	0.19	0.17
MgO	10.38	11.39	4.75	9.95	13.63	12.68	12.32	10.43	12.48	4.92	5.48	6.17	5.03	4.87	4.75
CaO	11.04	10.42	10.13	11.81	11.14	11.16	10.63	11.7	12.11	11.02	10.77	11.11	10.29	10.83	10.20
Na_2O	2.82	2.70	3.91	2.71	2.57	2.46	2.69	3.03	2.56	3.47	3.21	3.32	3.53	3.36	3.50
K_2O	0.97	1.07	1.61	0.95	0.89	0.90	1.02	1.03	0.8	1.16	1.27	1.23	1.32	1.38	1.40
P_2O_5	0.42	0.42	0.44	0.40	0.32	0.35	0.39	0.37	0.28	0.50	0.55	0.55	0.58	0.63	0.49
LOI	0.61	0.43	0.13	-0.38	-0.38	0.34	-0.43	-0.61	-0.08	-0.5	0.41	-0.43	0.73	0.17	0.33
Total	100.2	100.2	99.52	98.20	98.80	100.6	99.31	99.00	99.38	99.46	99.51	98.83	100.1	99.84	99.09
Sc	27	27	19	32	33	32	30	31	37	24	24	26	25	23	17
V	254	241	258	288	233	253	230	262	258	287	301	306	316	311	268
Cr	310	570	12	-	-	640	-	-	-	20	30	50	50	-	-
Co	45	51	37	-	-	51	-	-	-	35	39	42	36	37	36
Ni	210	290	52	167	294	270	252	183	229	80	100	110	80	80	80
Cu	80	60	64	60	41	40	38	49	38	70	80	80	80	90	70
Zn	90	90	91	75	70	80	79	71	67	110	110	110	120	110	100
Ga	17	18	23	-	-	17	-	-	-	22	21	22	23	22	22
Ge	1.0	1.0		-	-	2.0	-	-	-	1.0	1.0	1.0	2.0	1.0	1.0
Rb	19.0	22.0	24.0	-	-	19.0	-	-	-	23.0	25.0	24.0	28.0	27.0	27.0
Sr	512	503	697	481	415	444	480	513	350	585	626	624	544	677	690
Y	21.0	19.0	30.0	24	19	19.0	20	20	18	27.0	27.0	26.0	29.0	29.0	25.0
Zr	169	188	228	172	152	158	-	-	-	239	255	250	266	278	214
Nb	27.0	29.0	44.0	-	-	27.0	-	-	-	35.0	40.0	40.0	43.0	45.0	37.0
Ba	276	322	389	242	225	249	274	259	193	308	340	336	333	375	381
La	24.0	28.1	29.2	-	-	21.8	-	-	-	30.5	35.7	35.2	35.1	38.5	31.6
Ce	51.30	59.60	76.00	-	-	45.60	-	-	-	65.90	77.20	75.70	75.40	84.90	66.30
Pr	6.41	7.44	6.83	-	-	5.63	-	-	-	8.27	9.57	9.47	9.35	10.40	8.22
Nd	25.30	29.40	30.70	-	-	23.80	-	-	-	34.00	38.90	38.10	38.50	42.10	33.30
Sm	5.8	6.3	7.2	-	-	5.4	-	-	-	7.9	8.5	8.4	8.6	9.0	7.1
Eu	1.90	2.03	2.13	-	-	1.83	-	-	-	2.61	2.82	2.78	2.90	2.99	2.41
Gd	5.40	5.70	6.35	-	-	5.40	-	-	-	7.20	7.80	7.60	8.40	8.30	6.70

Tb	0.90	0.80	1.05	-	-	0.80	-	-	-	1.10	1.10	1.20	1.20	1.30	1.00
Dy	4.60	4.70	5.67	-	-	4.60	-	-	-	6.00	6.30	6.10	6.80	6.80	5.70
Ho	0.90	0.80	1.03	-	-	0.80	-	-	-	1.10	1.10	1.10	1.20	1.20	1.00
Er	2.20	2.20	2.73	-	-	2.10	-	-	-	2.90	3.00	2.90	3.20	3.10	2.70
Tm	0.29	0.29	0.38	-	-	0.28	-	-	-	0.38	0.40	0.38	0.43	0.42	0.36
Yb	1.80	1.80	2.20	-	-	1.70	-	-	-	2.30	2.30	2.30	2.60	2.50	2.20
Lu	0.27	0.25	0.32	-	-	0.27	-	-	-	0.33	0.35	0.34	0.37	0.37	0.32
Hf	3.80	4.30	5.20	-	-	3.70	-	-	-	5.10	5.70	5.50	6.00	6.10	4.60
Ta	1.90	2.10	2.84	-	-	1.80	-	-	-	2.40	2.80	2.80	2.80	3.00	2.50
Pb	6.00	-	-	-	-	-	-	-	-	-	-	-	6.00	-	-
Th	2.30	2.80	3.20	-	-	2.00	-	-	-	3.00	3.50	3.40	3.70	3.90	2.90
U	0.80	1.00	1.00	-	-	0.70	-	-	-	1.00	1.20	1.20	1.30	1.30	1.00
CaO/Al_2O_3	0.81	0.79	0.60	0.94	0.98	0.91	0.88	0.89	1.12	0.68	0.68	0.74	0.67	0.67	0.59
FeO_{tot}/MgO	0.94	0.88	2.37	1.01	0.74	0.79	0.79	0.96	0.79	2.13	2.00	1.78	2.31	2.34	2.13

Table 3

Click here to download Table: Table 3 - Microthermometry_AP.docx

Table 34. Microthermometry data

Study area	sample	olivines analysed	N° measures	Th (°C)	ρ (kg·m^{-3})
N120° system	*Pic12b*	*8*	*226*	*Th_L 23.2-31.0*	*737-513*
	Pic65s	2	62	Th_V 31.0 Th_L 24.7-30.2	461 583-715
	Pic85	1	43	Th_L 27.6-31.1	466-665
	Pic86	1	48	Th_L 26.2-28.0	656-691
	Pic90	1	48	Th_L 27-29.3	622-677
N60° system	*Pic22*	*1*	*1*	*Th_L 29.8*	*602*
	Pic32	*1*	*83*	*Th_L 24.8-30.2*	*586-714*
	Pic43s	2	14	Th_V 31.0 Th_L 26.8-31.0	461 475-680
	Pic69s	2	16	Th_L 26.9-30.8	537-678
	Pic70s	2	68	Th_L 27.8-31.0	475-660
	Pic87	1	12	Th_V 30.2-31.1	352-422
Lomba do Fogo-São João fault	*Pic15*	*5*	*250*	*Th_V 27.4-31.0* *Th_L 28.5-31.6*	*278-466* *513-644*
	Pic16	*3*	*95*	*Th_L 28.6-30.9*	*520-642*
	Pic19b	*3*	*279*	*Th_L 23.5-30.3*	*581-733*
	Pic58	*3*	*117*	*Th_L 23.2-31.0*	*520-736*
central crater	*Pic61*	*2*	*22*	*Th_L 26.0-30.7*	*548-694*
	Pic64	*1*	*44*	*Th_L 23.0-28.5*	*643-738*
	Pic66s	2	17	Th_L 27.2-30.8	537-672
	Pic83	1	9	Th_V 27.5-31.0	279-422
	Pic84	1	99	Th_L 28.5-31.1	466-644
	Pic89	1	30	Th_L 29.0-30.5	569-629

Table 4
Click here to download Table: Table 4 - mass-balance_AP.docx

Table ~~4~~3. Mass-balance calculations

step	starting comp.	final comp.	olivine comp.	clinopyroxene comp.	plagioclase comp.
1a: *from SMI1 to type A*	*D-5b**	*Pic87*	*ol4Pic32*	*cpx3Pic32*	
SiO_2	46.82	46.77	39.84	51.24	
TiO_2	3.64	2.01		1.16	
Al_2O_3	15.56	11.38		4.41	
Fe_2O_3	1.36	1.71		0.33	
FeO	6.80	8.56	14.15	4.89	
MnO	0.10	0.16	0.18	0.08	
MgO	5.77	13.63	46.79	15.46	
CaO	11.55	11.14	0.30	22.07	
Na_2O	3.61	2.57		0.31	
K_2O	1.00	0.89		0.02	
Mg#			*0.855*	*0.849*	
An					
Mode/Vol			*+9.5%*	*+17.5%*	
1b: *from SMI2 to type A*	*D-2*	*Pic87*	*ol4Pic32*	*cpx3Pic32*	
SiO_2	45.57	46.77	39.84	51.24	
TiO_2	3.94	2.01		1.16	
Al_2O_3	16.41	11.38		4.41	
Fe_2O_3	1.58	1.71		0.33	
FeO	7.52	8.56	14.15	4.89	
MnO	0.16	0.16	0.18	0.08	
MgO	5.72	13.63	46.79	15.46	
CaO	10.15	11.14	0.30	22.07	
Na_2O	3.44	2.57		0.31	
K_2O	1.28	0.89		0.02	
Mg#			*0.855*	*0.849*	
An					
Mode/Vol			+11%	+28.5%	

step	starting comp.	final comp.	olivine comp.	clinopyroxene comp.	plagioclase comp.
2: *from SMI1 to type B*	*D-5b**	*Pic68*	*ol4Pic32*	*cpx3Pic32*	*plg5Pic19b*
SiO_2	46.82	45.93	39.84	51.24	52.65
TiO_2	3.64	3.57		1.16	
Al_2O_3	15.56	16.26		4.41	29.54
Fe_2O_3	1.36	1.93		0.33	0.50
FeO	6.80	9.65	14.15	4.89	
MnO	0.10	0.19	0.18	0.08	
MgO	5.77	4.87	46.79	15.46	0.08
CaO	11.55	10.83	0.30	22.07	12.46
Na_2O	3.61	3.36		0.31	4.31
K_2O	1.00	1.38		0.02	0.24
Mg#			*0.855*	*0.849*	
An					*0.660*
Mode/Vol			*-3.4%*	*-4%*	*+2.5%*

*Data from Métrich et al. (2014)

Mg# = Mg/(Mg+Fe^{+2}) modal

An = Ca/(Ca+Na+K) modal

Table 5
Click here to download Table: Table 5 - TRAPPING EVENTS.docx

TABLE 5. Trapping/re-equilibration events

system	sample	density ρ (kg·m^-3)	ρ max	1st peak	2nd peak	3rd peak	4th peak	5th peak	6th peak	7th peak	8th peak	9th peak	10th peak	11th peak
Lomba do Fogo-São João fault	**Pic19**	ρ original	733	708±2	677±2									
		ρ (recalculated)	766	740	708									
		P *(MPa)*	489	459	419									
		depth *(km)*	**17.28**	**16.33**	**15.06**									
	Pic16-Pic58	ρ original	736	708					592	520				
		ρ (recalculated)	769	740					619	544				
		P *(MPa)*	497	459					319	251				
		depth *(km)*	**17.53**	**16.33**					**11.81**	**9.37**				
	Pic15	ρ original					644	627±2			466		382	
		ρ (recalculated)					673	656			487		399	
		P *(MPa)*					378	358			209		165	
		depth *(km)*					**13.76**	**13.12**			**7.86**		**6.21**	
N60° system	**Pic22-**Pic32-Pic87	ρ original		714		660±2		622±8				416	380	
		ρ (recalculated)		746		690		650				435	397	
		P *(MPa)*		467		397		352				180	164	
		depth *(km)*		**16.58**		**14.36**		**12.93**				**6.77**	**6.17**	
	Pic69s	ρ original							565±2					
		ρ (recalculated)							591					
		P *(MPa)*							292					
		depth *(km)*							**10.84**					
	Pic70-Pic43s	ρ original				656		629±2	548	536±2	475			
		ρ (recalculated)				686		658	573	560	497			
		P *(MPa)*				393		361	275	264	216			
		depth *(km)*				**14.23**		**13.22**	**10.23**	**9.84**	**8.12**			
N120° system	**Pic12**	ρ original	737	712	684±2			629±2						
		ρ (recalculated)	770	744	715			658						
		P *(MPa)*	498	464	428			361						
		depth *(km)*	**17.57**	**16.49**	**15.34**			**13.22**						
	Pic85-Pic86	ρ original			685±2		636±6			532				
		ρ (recalculated)			716		665			556				
		P *(MPa)*			429		368			261				
		depth *(km)*			**15.38**		**13.44**			**9.73**				
	Pic65-Pic90	ρ original		715		662±8					461			
		ρ (recalculated)		748		692					482			
		P *(MPa)*		470		400					206			
		depth *(km)*		**16.68**		**14.46**					**7.75**			
central crater	**Pic64-**Pic83	ρ original	738				643					416		330
		ρ (recalculated)	772				672					435		345
		P *(MPa)*	501				376					180		150
		depth *(km)*	**17.66**				**13.59**					**6.77**		**5.65**
	Pic84-Pic89	ρ original				655			602±2					
		ρ (recalculated)				685			629					
		P *(MPa)*				391			329					
		depth *(km)*				**14.17**			**12.16**					
	Pic61-Pic66s	ρ original			672				604±4					
		ρ (recalculated)			703				631					
		P *(MPa)*			413				331					
		depth *(km)*			**14.87**				**12.24**					